

Analytical estimation of emission zone mean position and width in organic light-emitting diodes from emission pattern image-source interference fringes

Ariel Epstein, Matthew Roberts, Nir Tessler, and Pinchas D. Einziger

Citation: [Journal of Applied Physics](#) **115**, 223101 (2014); doi: 10.1063/1.4880737

View online: <http://dx.doi.org/10.1063/1.4880737>

View Table of Contents: <http://scitation.aip.org/content/aip/journal/jap/115/22?ver=pdfcov>

Published by the [AIP Publishing](#)

Articles you may be interested in

[Low-voltage polariton electroluminescence from an ultrastrongly coupled organic light-emitting diode](#)

Appl. Phys. Lett. **104**, 233302 (2014); 10.1063/1.4871271

[Color-tunable and high-efficiency organic light-emitting diode by adjusting exciton bilateral migration zone](#)

Appl. Phys. Lett. **103**, 133307 (2013); 10.1063/1.4823476

[High-brightness, high-color-purity, white organic light-emitting diodes featuring multiple emission layers](#)

J. Appl. Phys. **105**, 064318 (2009); 10.1063/1.3097285

[White organic light-emitting diodes with fine chromaticity tuning via ultrathin layer position shifting](#)

Appl. Phys. Lett. **89**, 183513 (2006); 10.1063/1.2382730

[Determination of the width of the carrier recombination zone in organic light-emitting diodes](#)

J. Appl. Phys. **94**, 7764 (2003); 10.1063/1.1624477



Re-register for Table of Content Alerts

Create a profile.



Sign up today!



Analytical estimation of emission zone mean position and width in organic light-emitting diodes from emission pattern image-source interference fringes

Ariel Epstein,^{1,a)} Matthew Roberts,^{2,b)} Nir Tessler,^{1,c)} and Pinchas D. Einziger¹

¹*Department of Electrical Engineering, Technion-Israel Institute of Technology, Haifa 32000, Israel*

²*Cambridge Display Technology Ltd, Building 2020, Cambourne Business Park, Cambourne, Cambridgeshire CB23 6DW, United Kingdom*

(Received 26 October 2013; accepted 19 May 2014; published online 10 June 2014)

We present an analytical method for evaluating the first and second moments of the effective exciton spatial distribution in organic light-emitting diodes (OLED) from measured emission patterns. Specifically, the suggested algorithm estimates the emission zone mean position and width, respectively, from two distinct features of the pattern produced by interference between the emission sources and their images (induced by the reflective cathode): the angles in which interference extrema are observed, and the prominence of interference fringes. The relations between these parameters are derived rigorously for a general OLED structure, indicating that extrema angles are related to the mean position of the radiating excitons via Bragg's condition, and the spatial broadening is related to the attenuation of the image-source interference prominence due to an averaging effect. The method is applied successfully both on simulated emission patterns and on experimental data, exhibiting a very good agreement with the results obtained by numerical techniques. We investigate the method performance in detail, showing that it is capable of producing accurate estimations for a wide range of source-cathode separation distances, provided that the measured spectral interval is large enough; guidelines for achieving reliable evaluations are deduced from these results as well. As opposed to numerical fitting tools employed to perform similar tasks to date, our approximate method explicitly utilizes physical intuition and requires far less computational effort (no fitting is involved). Hence, applications that do not require highly resolved estimations, e.g., preliminary design and production-line verification, can benefit substantially from the analytical algorithm, when applicable. This introduces a novel set of efficient tools for OLED engineering, highly important in the view of the crucial role the exciton distribution plays in determining the device performance. © 2014 AIP Publishing LLC. [<http://dx.doi.org/10.1063/1.4880737>]

I. INTRODUCTION

Organic light-emitting diodes (OLED) technology has advanced immensely over the past two decades. Overcoming the spin statistics problem by combining phosphorescent emitters in active layers, and introduction of doped transport layers have improved dramatically the electrical properties of the devices, enabling realizable designs with almost 100% internal quantum efficiency (IQE).^{1–3} In contrast, the optical properties of the devices are still far from optimal, limiting external quantum efficiencies (EQE) to ~20% in standard OLEDs.^{4,5} It is well established by now that the optical properties of OLEDs, in particular, the outcoupling efficiency, are strongly dependent on the spatial distribution of the radiating excitons in the active layer and their orientation preference (if exists).^{6–12} Consequently, accessing these emission zone (EZ) properties by optical means has become highly desirable, as it offers an efficient way to evaluate these important parameters

during the research and development process, or as quality control at the manufacturing line. Moreover, as the emission zone profile is determined by the electrical characteristics of the device (charge carrier mobilities, diffusion coefficients, injection barriers, etc.),¹³ such tools also provide an effective way to investigate the charge transport properties of the device, which are still subject to intensive studies.^{3,14}

Indeed, in the last couple of years numerous authors have presented methods to recover EZ properties from a variety of optical measurements, such as electroluminescence (EL) spectra, emission patterns, external efficiencies, and photoluminescence lifetimes.^{12,15–21} These methods heavily utilize fitting procedures, which may yield highly resolved evaluation, however, usually require extensive data sets, and naturally rely on advanced numerical techniques, which tend to obscure the underlying physical phenomena.^{19,22,23} In recent work, we have presented a different approach to this problem, developing analytical closed-form formulae to extract the emission zone location from measured emission pattern extrema, assuming the excitons are concentrated in a very narrow region.²⁴ We have shown therein that the angles in which maximum or minimum emission occurs are related to the emitter location via a generalized Bragg's condition,

^{a)}ariel.epstein@utoronto.ca. Present address: Edward S. Rogers Sr. Department of Electrical and Computer Engineering, University of Toronto, Toronto, Ontario M5S 2E4, Canada.

^{b)}mroberts@cdtltd.co.uk

^{c)}nir@ee.technion.ac.il

which stems from the interference between the radiating source and its image, induced by the reflecting cathode. The resultant set of expressions allows evaluation of the emission zone location by a simple back-of-an-envelope calculation, requiring only a knowledge of the local extremum angles and the optical constants of the various layers at a single wavelength.²⁵ As expected from an analytical approach, the method we have presented relies on a focused set of measurements, requires little computation power (no fitting is involved), and reflects the dominant physical processes.

Nonetheless, that efficient method relies on several simplifying assumptions which are not always satisfied: first, a very narrow emission zone was assumed, neglecting any spatial broadening effects; second, we have assumed that the anode and the organic layers in the device have similar optical properties; and third, the presented algorithm relied on a simplified formulation, using 2D line sources instead of 3D point dipoles.²⁶

In this paper, we augment our previous work to allow a more detailed and accurate estimation of the EZ properties, including emission zone mean position and width, while preserving the key advantages of an analytical approach. The method is based on three analytical steps, employed on the measured transverse electric (TE) polarized emission pattern,²⁷ which is less sensitive to the dipole orientation.^{18,20,22} First, we apply a simple division operation to the measured emission pattern to isolate the image-source (IS) interference term. Second, we apply a simplified form of our previous theory to determine the mean value of the exciton spatial distribution from Bragg's condition. The third step utilizes the extracted EZ mean position and the ratio between forward and side-lobe emission to estimate the EZ width from the extent of averaging that the pattern exhibits. In addition, we indicate the precise steps that should be taken to distinguish between the contributions of the horizontal and vertical dipoles to the transverse magnetic (TM) polarized emission, utilizing the difference in intrinsic emission patterns of the two species and the EZ profile evaluated in previous steps; however, a detailed investigation of this last step is beyond the scope of this paper.

Before we dive into the rigorous formulation, it is worthwhile to emphasize the two main merits of our approximate method, in view of the availability of highly accurate numerical tools.^{12,15–22} First, for some OLED engineering tasks, the complexity involved in employing the numerical methods is not very cost effective. For initial design stages and routine verification processes, for instance, it seems that a more intuitive, computationally efficient, approach, as the one presented in this paper, would be a better choice. The latter allows faster trial-and-error cycles in preliminary design steps, and a means to simply predict how changes in the electrical properties of the OLEDs are manifested in measured emission patterns, facilitating simple monitoring of production discrepancies. In addition, the physical insight provided by the analytical derivation highlights the features most sensitive to emission zone variations, thus enabling application to standard OLEDs, without the necessity to specially design them for emission zone investigation.¹⁸

Second, even though several steps in the analytical algorithm require pre-processing effort, and we make use of a

computer program to implement those for repeated automatic analyses, this is completely different, both conceptually and computationally, from implementing a numerical fitting tool. The former relies on prescribed closed-form formulae utilizing *two* physically meaningful optical parameters of a *monochromatic* emission pattern; the latter involves a feedback process between a trial EZ profile with free parameters, an optical simulation, and measured data, which is usually required to be as detailed as possible to promote convergence to a reliable estimation.^{17–19,28} Thus, fitting procedures are much more computationally and experimentally demanding than the proposed analytical method.

The rest of the paper is arranged as follows. Section II opens with statement of the model assumptions, followed by the analytical formulation of OLED polarized emission patterns (Subsection II A), and derivation of the relations between the latter and the main features of the emission zone (Subsection II B); these form the analytical estimation procedure. Appendix A and Appendix B describe how thick layers and interlayers (ILs) between the cathode and active layer, respectively, should be integrated into the model; while Appendix C suggests a path for estimating the orientation of the emitting dipoles. In Section III, we verify our method by application to simulated (Subsection III A) and measured (Subsection III B) results; important discussions regarding the usage of the method are included in these Subsections as well. The software tool utilized in Sec. III to implement the estimation method is described in detail in Appendix D. Lastly, Sec. IV summarizes our main conclusions.

II. THEORY

In this section, we rigorously establish closed-form analytical expressions for the polarized emission patterns of a general OLED configuration, first for a single dipole (Subsection II A 1), and then for the exciton ensemble (Subsection II A 2). Subsection II B formulates the analytical estimation procedure: the structured form of the emission pattern expressions (Eq. (1)) is utilized to isolate the IS interference factor (Eq. (15)); in Subsection II B 1, the EZ mean position is evaluated from the measured IS interference extremum angles (Eq. (23)); and in Subsection II B 2, the EZ width is estimated from the measured IS interference fringe prominence (Eq. (26)).

The resultant estimation procedure, summarized in Table I, utilizes three main assumptions:

1. The active layer is adjacent to the cathode. This simplifies the derivation of Bragg's condition for the interference between the source and its image (Eq. (23)); generalization of the method to other configurations is discussed in Appendix B.
2. Some of the measured monochromatic IS patterns exhibit local extrema; this is required for the application of our algorithm and should be achieved by collecting data from a wide spectral range (see Subsection III A).
3. The exciton distribution is not very wide with respect to the wavelength. This is essential to establish the analytical estimation process, enabling description of the distribution function via its mean position and width alone (Eq.

TABLE I. Summary of the analytical estimation method formulated in Sec. II.

No.	Step	Input	Output	Relevant equations
1	Image-source interference	Measured TE emission pattern: $E_{S_r}(\theta; \omega)$ OLED configuration: $d_n, \epsilon_n, \mu_n, \sigma_n$	IS interference pattern: $E_{T_{IS}}(\theta; \omega)$ Extrema angles: $\theta_{\max}, \theta_{\min}$ Fringe prominence: \mathcal{P}	(10), (12), (15), and (24)
2	Emission zone mean position	Extrema angles: $\theta_{\max}, \theta_{\min}$ Active layer and cathode properties: k_1, k_{-2}	Emission zone mean position: $\langle z' \rangle$	(6), (21), and (23)
3	Emission zone width	Extrema angles: $\theta_{\max}, \theta_{\min}$ Active layer and cathode properties: k_1, k_{-2} Emission zone mean position: $\langle z' \rangle$ Fringe prominence: \mathcal{P}	Emission zone width: W	(25)–(27)

(17)), as well as decoupling between the effect of the two on the IS pattern (Eqs. (19) and (20)).

This last assumption implies that the estimation accuracy is expected to drop for emission zone profiles which are very wide or with a highly asymmetrical spatial variation, inducing dominant high order moments. In practice, however, the range of device parameters for which the method performs well is quite large, and may account for a variety of device configurations and emission zones; this shall be demonstrated in Sec. III.

A. Emission pattern formulation

We consider a prototype device with $N+2$ distinct layers. An electric dipole of dipole moment ${}^e I_0 l$ is embedded at a certain plane, $z = z'$, sandwiched between layers (-1) and $(+1)$, forming an angle of α with the negative z -axis (Fig. 1). The emission pattern measured for the actual device would be a superposition of the emission of various such dipoles, distributed along the active layer and having various orientations following the characteristic spatial and orientation distribution functions of the realistic device.^{18,20} The prototype configuration consists of a metallic cathode, an organic active layer containing the emitting excitons, a stack of additional organic layers, and a transparent anode, all fabricated on a thick transparent substrate (Sec. II/Assumption 1); the far-field observation point \vec{r} lies in air, forming an angle of θ with the z -axis.

Each layer is characterized by its permittivity, permeability, and conductivity, given for the n th layer by ϵ_n, μ_n , and σ_n , respectively; in the active layer, $\epsilon_{-1} = \epsilon_1, \mu_{-1} = \mu_1$, and $\sigma_{-1} = \sigma_1$. Considering a time-harmonic excitation with time dependence $e^{j\omega t}$, the wave number of the n th layer is

given by $k_n = \omega \sqrt{\mu_n \epsilon_n [1 - j\sigma_n / (\omega \epsilon_n)]} = (\omega/c)(n_n - j\kappa_n)$, where c is the speed of light in vacuum, and n_n and κ_n denote the refractive index and extinction coefficient of the n th layer, respectively; the wave impedance is defined as $Z_n = \omega \mu_n / k_n$. Our formulation is based on decomposition of the currents and fields to their plane-wave spectrum,^{9,29–32} where we use the common notation of k_t and $\beta_n = \sqrt{k_n^2 - k_t^2}$ for the transverse and longitudinal components of the wave number in the n th layer, respectively.^{6,9,33,34} To satisfy the radiation condition, we demand that $\Im\{k_n\} \leq 0$ and $\Im\{\beta_n\} \leq 0$.

1. Emission pattern of a single dipole

The first step in evaluating the emission pattern of the tilted current element of Fig. 1 is to decompose it into a vertical electric dipole (VED) of magnitude ${}^e I_0^\perp l = {}^e I_0 l \cos \alpha$, producing only TM-polarized emission ($H_z = 0$), and an horizontal electric dipole (HED) of magnitude ${}^e I_0^\parallel l = {}^e I_0 l \sin \alpha$, contributing to both TM-polarized ($H_z = 0$) and TE-polarized ($E_z = 0$) emission.^{6,9,27,33,34} Following previous work,^{30,31,35} we further decompose the latter into TE-generating current element and TM-generating current element, which allows an elegant derivation of the polarized emission pattern of the device, defined as the projection of the Poynting vector on the observation direction \hat{r} . This procedure leads to the identification of three primitive source species: the TM-generating VED, denoted by \perp and M superscripts, the TE-generating component of the HED, denoted by \parallel and E superscripts, and the TM-generating component of the HED, denoted by \parallel and M superscripts, throughout the paper. The individual (orthogonal) emission patterns of these primitive species can be formulated in a unified manner^{30,31}

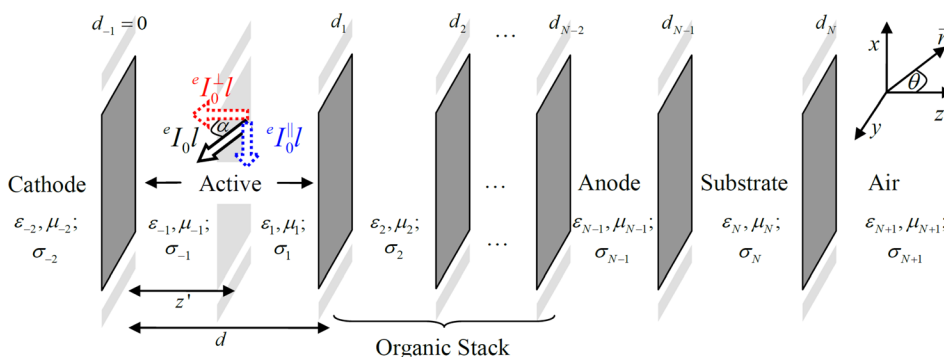


FIG. 1. Physical configuration of a typical OLED. An arbitrarily oriented dipole (black hollow arrow) is decomposed to a horizontal dipole (blue dotted hollow arrow) and a vertical dipole (red dotted hollow arrow).

$$S_r(\theta; z', \omega) = \frac{P_{N+1}}{4\pi r^2} \times \frac{3\xi(k_t)}{2} T_{IS}(k_t, z') T_{DR}(k_t) T_{WM}(k_t) \Big|_{k_t = k_{N+1} \sin \theta}, \quad (1)$$

where $P_n = Z_n |e I_0 k_n l|^2 / (12\pi)$ is the power radiated by an electric dipole in unbounded medium, and r is the distance between the origin and the observation point; the IS, direct-ray (DR), and weak-microcavity (WM) contributions are given, respectively, by⁹

$$T_{IS}(k_t, z') = 1 + |\widehat{\Gamma}_{-1}(k_t)|^2 - 2\Re\{\widehat{\Gamma}_{-1}(k_t) e^{-2j\beta\{d_1\}(z'-d_1)}\}, \quad (2)$$

$$T_{DR}(k_t) = |1 + \Gamma_1(k_t)|^2 \times \prod_{n=1}^{N-1} |1 + \Gamma_{n+1}(k_t) e^{-j\beta_{n+1}(d_{n+1}-d_n)}|^2, \quad (3)$$

$$T_{WM}(k_t) = \frac{1}{|1 - \widehat{\Gamma}_{-1}(k_t) R_1(k_t) e^{-2j\beta_1(d_1-d_1)}|^2} \times \prod_{n=1}^{N-1} \frac{1}{|1 + \Gamma_n(k_t) R_{n+1}(k_t) e^{-2j\beta_{n+1}(d_{n+1}-d_n)}|^2}, \quad (4)$$

and $\Gamma_n(k_t)$ and $R_n(k_t)$ are, respectively, the local and total reflection coefficients at the n th interface, in the forward direction. The local reflection coefficients consider only the reflection due to the discontinuity between the n th and the $(n+1)$ th media, whereas the total reflection coefficients take into account the overall reflection due to the stack of layers to the right of the n th interface, including multiple reflections (Fig. 1). Therefore, the total reflection coefficients are recursively defined via

$$\begin{cases} R_n(k_t) = \frac{\Gamma_n(k_t) + R_{n+1}(k_t) e^{-2j\beta_{n+1}(d_{n+1}-d_n)}}{1 + \Gamma_n(k_t) R_{n+1}(k_t) e^{-2j\beta_{n+1}(d_{n+1}-d_n)}} \\ R_{N+1}(k_t) = 0, \end{cases} \quad (5)$$

while the local reflection coefficients are given by the Fresnel formula, $\Gamma_n = (1 - \gamma_n)/(1 + \gamma_n)$, where γ_n is the generalized impedance ratio around the n th interface. Due to the difference in boundary conditions, γ_n must be defined separately for each of the primitive sources,^{9,30,31}

$${}^M \gamma_n^\perp = \frac{k_{n+1} \beta_n}{k_n \beta_{n+1}} \left(\frac{Z_{n+1}}{Z_n} \right)^{-1}, \quad {}^E \gamma_n^\parallel = \left(\frac{k_{n+1} \beta_n}{k_n \beta_{n+1}} \right)^{\pm 1} \frac{Z_{n+1}}{Z_n}, \quad (6)$$

and we also define the local reflection coefficients in the reversed direction as³⁶

$$\widehat{\Gamma}_n(k_t) = \begin{cases} -\Gamma_n(k_t) & n > 0 \\ -\Gamma_{n-1}(k_t) & n < 0. \end{cases} \quad (7)$$

Besides the difference in local reflection coefficients, the different orientation of the primitive sources also induces a difference in their emission patterns (e.g., it is known that dipoles do not radiate parallel to their moment). This effect is introduced to Eq. (1) by the orientation factor, $\xi(k_t)$, given for the various sources by^{30,31}

$${}^M \xi^\perp(k_t) = \left(\frac{k_t}{k_{N+1}} \right)^2, \quad {}^E \xi^\parallel(k_t) = \frac{1}{2} \left(\frac{\beta_{N+1}}{k_{N+1}} \right)^{1 \mp 1}, \quad (8)$$

where we have considered the dipole moments to have no azimuthal preference for their orientation (i.e., the φ dependence of the dipoles is averaged).^{30,33,34}

The emission pattern of a dipole tilted by α with respect to the z -axis (Fig. 1) is thus given as a superposition of the three orthogonal contributions, namely,

$$S_r(\theta; \alpha, z', \omega) = {}^M S_r^\perp(\theta; z', \omega) \cos^2 \alpha + \left[{}^E S_r^\parallel(\theta; z', \omega) + {}^M S_r^\parallel(\theta; z', \omega) \right] \sin^2 \alpha. \quad (9)$$

In many instances, the OLED stack contains at least one layer (the substrate, usually) which is much thicker than the coherence length exhibited by measurement spectral resolution or emitter ensemble.^{9,37} In such cases, the measured emission pattern would not be consistent with Eq. (9), and the coherence length effect should be properly incorporated into the model. In order not to interfere with the fluency of reading, the modifications required to facilitate this incorporation, and the final results, are detailed in Appendix A.

2. Emission pattern of the dipole ensemble

We may now formulate an expression for the measured spectrally resolved polarized emission pattern of the entire (spatially incoherent³⁸) exciton ensemble by integrating the respective terms of Eq. (9) over the spatial distribution of the excitons, $f(z')$, and their orientation distribution, $h(\alpha)$, yielding²⁰

$${}^E S_r(\theta; \omega) = p(\omega) \int_{d_1}^{d_1} dz' \int_0^{\pi/2} d\alpha \left[\frac{f(z') h(\alpha) \sin \alpha \cdot \eta_{\text{ext}}(z', \alpha, \omega)}{{}^E S_r^\parallel(\theta; z', \omega) \sin^2 \alpha} \right], \quad (10)$$

$${}^M S_r(\theta; \omega) = p(\omega) \int_{d_1}^{d_1} dz' \int_0^{\pi/2} d\alpha \left[\frac{f(z') h(\alpha) \sin \alpha \cdot \eta_{\text{ext}}(z', \alpha, \omega)}{[{}^M S_r^\parallel(\theta; z', \omega) \sin^2 \alpha + {}^M S_r^\perp(\theta; z', \omega) \cos^2 \alpha]} \right], \quad (11)$$

for TE-polarized and TM-polarized emission, respectively. The parameter $\eta_{\text{ext}}(z', \alpha, \omega)$ relates to the EQE of a dipole tilted by α with respect to the z -axis, radiating from the plane $z = z'$ at an angular frequency ω . It is determined by the internal quantum efficiency of such a dipole, which considers electrical losses and non-classical decay channels, multiplied by the ratio between the power radiated by the dipole (both TE and TM polarizations, all angles considered) to free space (layer $N+1$ in our formulation) and the total power dissipation of the dipole (e.g., also to waveguided, substrate, and surface-plasmon modes).²⁰ The spectral distribution of the sources $p(\omega)$ acts as spectral weight function to the nominal power radiated by a single dipole in unbounded medium P_{N+1} (Eq. (1)). The distribution functions must satisfy normalization conditions, namely, $\int_0^{\pi/2} d\alpha \sin \alpha h(\alpha) = \int_{d_1}^{d_1} dz' f(z') = 1$.

B. Emission zone evaluation

1. Emission zone mean position

After establishing the constituent relations for the polarized emission pattern, our first step is to evaluate the mean position of radiating exciton, i.e., the first moment of the effective exciton spatial distribution. To that end, we note that the effect of the dipole location on the primitive source emission pattern (Eq. (1)) arises only from the image-source transmission factor (Eq. (2)). Thus, we begin by decoupling this contribution from the measured emission pattern, defining the ensemble image-source contribution to the TE-polarized emission pattern as (Table I/step 1)

$$\begin{aligned} E_{T_{IS}}(\theta; \omega) &= \frac{E_{S_r}(\theta; \omega)}{\frac{3^E \zeta^{\parallel}(k_t)}{2} E_{T_{DR}}(k_t) E_{T_{WM}}(k_t)|_{k_t = k_{N+1} \sin \theta}} \\ &= p(\omega) \frac{P_{N+1}}{4\pi r^2} \int_{d_1}^{d_2} dz' f^{\parallel}(z') E_{T_{IS}}(k_t, z')|_{k_t = k_{N+1} \sin \theta} \\ &\quad \times \int_0^{\pi/2} d\alpha h(\alpha) \sin^3 \alpha \eta_{\text{ext}}(z', \alpha, \omega). \end{aligned} \quad (12)$$

$$E_{T_{IS}}(\theta; \omega) = p(\omega) \bar{\eta}_{\text{ext}}(\omega) \frac{P_{N+1}}{4\pi r^2} \times \left(1 + |\hat{\Gamma}_{-1}(k_t)|^2 - 2\Re \left\{ \hat{\Gamma}_{-1}(k_t) \int_0^d dz' \bar{f}^{\parallel}(z', \omega) e^{-2j\beta_1 z'} \right\} \right), \quad (15)$$

where we assumed that propagation losses in the active layer are negligible, and defined its width as $d = d_1 - d_{-1}$ (Fig. 1).

Next, we expand the integral in the third term in the parenthesis of Eq. (15) using the moments of $\bar{f}^{\parallel}(z', \omega)$,

$$\begin{aligned} \int_0^d dz' \bar{f}^{\parallel}(z', \omega) e^{-2j\beta_1 z'} &= e^{-2j\beta_1 \langle z' \rangle} \int_0^d dz' \bar{f}^{\parallel}(z', \omega) e^{-2j\beta_1 (z' - \langle z' \rangle)} \\ &= e^{-2j\beta_1 \langle z' \rangle} \int_0^d dz' \bar{f}^{\parallel}(z', \omega) \\ &\quad \times \sum_{m=0}^{\infty} \frac{(-2j\beta_1)^m}{m!} (z' - \langle z' \rangle)^m \\ &= e^{-2j\beta_1 \langle z' \rangle} \sum_{m=0}^{\infty} \frac{(-2j\beta_1)^m}{m!} E[(z' - \langle z' \rangle)^m], \end{aligned} \quad (16)$$

where $E[(z' - \langle z' \rangle)^m]$ is the m th moment of the function $\bar{f}^{\parallel}(z', \omega)$ about its expectation value $\langle z' \rangle$, and we assume the excitons are distributed on an interval smaller than the wavelength in the active layer, such that the summation converges. In fact, we further assume that the spatial distribution

We first evaluate formally the integral over the orientation angle, defining the effective contribution of the HEDs to the EQE, $\bar{\eta}_{\text{ext}}^{\parallel}(z', \omega)$, given the orientation distribution $h(\alpha)$ via

$$\bar{\eta}_{\text{ext}}^{\parallel}(z', \omega) = \int_0^{\pi/2} d\alpha h(\alpha) \sin^3 \alpha \eta_{\text{ext}}(z', \alpha, \omega), \quad (13)$$

using which we define the effective spatial HED distribution function

$$\bar{f}^{\parallel}(z', \omega) = f^{\parallel}(z') \bar{\eta}_{\text{ext}}^{\parallel}(z', \omega) / \bar{\eta}_{\text{ext}}^{\parallel}(\omega), \quad (14)$$

where the normalization factor $\bar{\eta}_{\text{ext}}^{\parallel}(\omega)$ is defined as to ensure that $\int_0^d dz' \bar{f}^{\parallel}(z', \omega) = 1$. It is worth noting at this point that our analytical method would result in an evaluation of the first and second moments of the *effective* distribution $\bar{f}^{\parallel}(z', \omega)$, which is the original exciton spatial distribution $f^{\parallel}(z')$ weighted by the relative EQE of the HEDs at $z = z'$, $\bar{\eta}_{\text{ext}}^{\parallel}(z', \omega) / \bar{\eta}_{\text{ext}}^{\parallel}(\omega)$. The consequences of this convolution between the spatial distribution and the orientation-dependent EQE would be discussed in Subsection III B 2.

Substituting these definitions into Eq. (12) yields

is such that it can be described well by its first two moments, and we neglect the higher order terms $m \geq 3$ in the moment series (Sec. II/Assumption 3). Noting that $E[(z' - \langle z' \rangle)] = 0$, and defining the distribution width W as its standard deviation $W^2 = E[(z' - \langle z' \rangle)^2]$, Eq. (16) transforms into

$$\int_0^d dz' \bar{f}^{\parallel}(z', \omega) e^{-2j\beta_1 z'} \approx e^{-2j\beta_1 \langle z' \rangle} \left[1 - \frac{1}{2} (2\beta_1 W)^2 \right]. \quad (17)$$

As implied in our previous work,^{9,24} the extrema angles of the IS interference fringes are closely related to the mean position of the emission zone. Thus, our second step involves finding the zeros of the derivative of the decoupled IS response Eq. (15) with respect to the wave-number in the active layer, $\beta_1 = k_1 \cos \theta_{\text{act}}$ (Sec. II/Assumption 2). The relation between β_1 and the observation angle θ is monotonic, and given by Snell's law $k_t = k_{N+1} \sin \theta = k_1 \sin \theta_{\text{act}}$, where θ_{act} is the propagation angle in the active layer. As the absolute value of the cathode/organic reflection coefficient $|\hat{\Gamma}_{-1}(k_t)|$ varies very little with the observation angle, we neglect its contribution to the derivative, and the IS interference extrema are thus given by the equation

$$\frac{\partial}{\partial \beta_1} \Re \left\{ \widehat{\Gamma}_{-1} e^{-2j\beta_1 \langle z' \rangle} \int_0^d dz' f^{\parallel}(z', \omega) e^{-2j\beta_1 (z' - \langle z' \rangle)} \right\} = 0, \quad (18)$$

which reads, using Eq. (17),

$$\Re \left\{ \left[\begin{array}{c} e^{-2j\beta_1 \langle z' \rangle} \\ \left[\left(\frac{\partial \widehat{\Gamma}_{-1}}{\partial \beta_1} - 2j \langle z' \rangle \widehat{\Gamma}_{-1} \right) \left(1 - \frac{1}{2} (2\beta_1 W)^2 \right) \right] \\ - \frac{\widehat{\Gamma}_{-1}}{\beta_1} (2\beta_1 W)^2 \end{array} \right] \right\} = 0. \quad (19)$$

Treating the spatial broadening as a perturbation $(2\beta_1 W)^2 \ll 1$ (Sec. II/Assumption 3), we neglect, as a zeroth order approximation, the contribution of the second term in the square brackets which leads us to

$$\Re \left\{ e^{-2j\beta_1 \langle z' \rangle} \frac{\widehat{\Gamma}_{-1}}{\beta_1} \left(\frac{\beta_1}{\widehat{\Gamma}_{-1}} \frac{\partial \widehat{\Gamma}_{-1}}{\partial \beta_1} - 2j\beta_1 \langle z' \rangle \right) \right\} = 0, \quad (20)$$

which relates $\langle z' \rangle$ to the observation angles in which IS interference extrema occur (via β_1).

Similar to our previous work,²⁴ to facilitate the analytical solution of Eq. (20) we utilize the Leontovich surface impedance approximation³⁹ for the cathode/organic reflection coefficient, yielding,

$$\widehat{\Gamma}_{-1} = \frac{1 - (r_{\text{img}} \chi_{\text{act}})^2 - 2jr_{\text{img}} \chi_{\text{act}}}{1 + (r_{\text{img}} \chi_{\text{act}})^2}, \quad (21)$$

$$\frac{\beta_1}{\widehat{\Gamma}_{-1}} \frac{\partial \widehat{\Gamma}_{-1}}{\partial \beta_1} = - \frac{2jr_{\text{img}} \chi_{\text{act}}}{1 + (r_{\text{img}} \chi_{\text{act}})^2}, \quad (22)$$

where $r_{\text{img}} = n_1/\kappa_{-2}$ is the ratio between the active layer refractive index and the cathode extinction coefficient, and $\chi_{\text{act}} = \cos \theta_{\text{act}} = \beta_1/k_1$ is the projection of the propagation direction in the active layer on the z axis.²⁴

Finally, given the angles in which maxima or minima are observed in the decoupled IS interference pattern, the mean position of the radiating excitons can be evaluated via (Table I/step 2)

$$2k_1 \langle z' \rangle \chi_{\text{act}} + (\alpha_{\text{img}} - \alpha_0) = \begin{cases} 2\pi\nu + \pi & \text{local min} \\ 2\pi\nu & \text{local max,} \end{cases} \quad (23)$$

where, using the notations of Ref. 24, $(\alpha_{\text{img}} - \alpha_0)$ is the phase addition upon a single reflection at the cathode/organic interface for TE-polarized fields, given explicitly by $\tan \alpha_{\text{img}} = 2r_{\text{img}} \chi_{\text{act}} / [1 - (r_{\text{img}} \chi_{\text{act}})^2]$ and $\alpha_0 = \pi$. Actually, a more accurate evaluation of α_{img} is given by $\alpha_{\text{img}} = |\angle \widehat{\Gamma}_{-1}|$, i.e., the argument of the complex number $\widehat{\Gamma}_{-1}$. The extremum angles of the IS interference pattern θ_{ex} enter this condition via χ_{act} , which should be evaluated using the angles of local minima θ_{min} or local

maxima θ_{max} , according to the case considered. The parameter ν is an integer standing for the interference order; if the sources are positioned close to the cathode (on a wavelength scale), the $\nu=0$ is applicable; for thick active layers, solutions of higher order should be taken into account as well.

Indeed, Eq. (23) is a manifestation of Bragg's condition: it matches the phase accumulated during propagation from the source to the cathode and back (first term) added to the additional phase due to the reflection from the cathode/organic interface (second term), on the left-hand side (LHS) of the equation, to an integer number of full cycles (constructive interference) or full cycles and a half (destructive interference), on its right-hand side (RHS).

It is worth noting that although we have assumed that the active layer and the cathode are adjacent (Sec. II/Assumption 1), the relation between the local extrema and the EZ mean position can be generalized, in principle, for configurations which do not adhere to this limitation. The steps required for such generalization and its applicability are discussed in Appendix B.

2. Emission zone width

As demonstrated in Ref. 9, the finite width of the spatial distribution function gives rise to a spatial broadening attenuation factor, which reduces the relative contribution of the image-source interference cross-term to the overall emission pattern. This implies that the prominence of IS interference fringes will be diminished as the emission zone width grows, due to an averaging effect. Consequently, we utilize the mean EZ position evaluated in Subsection II B 1 to predict the fringe prominence that would have been measured if the EZ width was infinitesimally small; by comparing this reference fringe prominence to the measured value, we may estimate the EZ width in the OLED under test. The fringe prominence is defined, using Eqs. (15) and (17), as the measured forward to side-lobe emission ratio, namely

$$\mathcal{P} = \frac{E_{T_{IS}}(\theta = 0; \omega)}{E_{T_{IS}}(\theta = \theta_{\text{ex}}; \omega)} = \frac{\mathcal{I}_0 - \mathcal{X}_0 \left[1 - \frac{1}{2} (2k_1 \chi_{\text{act},0} W)^2 \right]}{\mathcal{I}_{\text{ex}} - \mathcal{X}_{\text{ex}} \left[1 - \frac{1}{2} (2k_1 \chi_{\text{act,ex}} W)^2 \right]}, \quad (24)$$

where the IS interference self and cross terms are defined, respectively, as

$$\begin{aligned} \mathcal{I}(\theta) &= \left[1 + |\widehat{\Gamma}_{-1}(k_t)|^2 \right]_{k_t = k_{N+1} \sin \theta} \\ \mathcal{X}(\theta) &= 2\Re \left\{ \widehat{\Gamma}_{-1}(k_t) e^{-2j\beta_1 \langle z' \rangle} \right\}_{k_t = k_{N+1} \sin \theta,} \end{aligned} \quad (25)$$

and the subscripts 0 and ex denote evaluation at $\theta=0$ and $\theta=\theta_{\text{ex}}$, respectively; the latter may correspond to angles of local minima θ_{min} or local maxima θ_{max} .

Equation (24) can be solved for the perturbation W^2 , yielding the desirable relation between the measured fringe

prominence and the spatial distribution width, namely, (Table I/step 3)

$$\frac{1}{2}(2k_1W)^2 = \frac{\mathcal{I}_0 - \mathcal{X}_0 - \mathcal{P}(\mathcal{I}_{\text{ex}} - \mathcal{X}_{\text{ex}})}{\mathcal{P}\mathcal{X}_{\text{ex}}(\lambda_{\text{act,ex}})^2 - \mathcal{X}_0(\lambda_{\text{act,0}})^2}. \quad (26)$$

It is worth noting that by defining the fringe prominence of an infinitesimally broadened emission zone as $\tilde{\mathcal{P}} = (\mathcal{I}_0 - \mathcal{X}_0)/(\mathcal{I}_{\text{ex}} - \mathcal{X}_{\text{ex}})$, we may rewrite Eq. (26) as

$$\frac{1}{2}(2k_1W)^2 = \frac{(\tilde{\mathcal{P}} - \mathcal{P})(\mathcal{I}_{\text{ex}} - \mathcal{X}_{\text{ex}})}{\mathcal{P}\mathcal{X}_{\text{ex}}(\lambda_{\text{act,ex}})^2 - \mathcal{X}_0(\lambda_{\text{act,0}})^2}, \quad (27)$$

indicating that similarity between the measured \mathcal{P} and reference $\tilde{\mathcal{P}}$ fringe prominence values would yield width estimations approaching zero, in consistency with our discussion in the beginning of this subsection.

The estimation procedure introduced in this section is summarized in Table I, with references to the equations relevant for each step. It is worth noting that after the EZ mean position and width are estimated from the measured TE-polarized emission pattern, their values can be utilized, in conjunction with TM-polarized measurements, to reveal information regarding the orientation distribution of the radiating excitons. The analytical steps to retrieve that information are listed in Appendix C; in-depth investigation of these further steps, however, is beyond the scope of this paper.

III. RESULTS AND DISCUSSION

A. Application of the method on simulated data

We first verify our method using simulated emission patterns of a prototype device, based on the device fabricated, characterized, and analyzed by Van Mensfoort *et al.*¹⁹ The prototype device consists of a glass substrate (1 mm), ITO anode (120 nm), PEDOT:PSS injection layer (100 nm), NRS-PPV active layer (200 nm), and an Aluminium cathode (Fig. 2). The spectral dependence of the refractive indices and extinction coefficients of the NRS-PPV and PEDOT:PSS were extracted from Ref. 19, of the ITO from Refs. 40–42, of the glass (non dispersive BK7) and aluminium from Ref. 43.

We have generated spectrally resolved TE-polarized emission patterns of the prototype device hosting symmetrical and

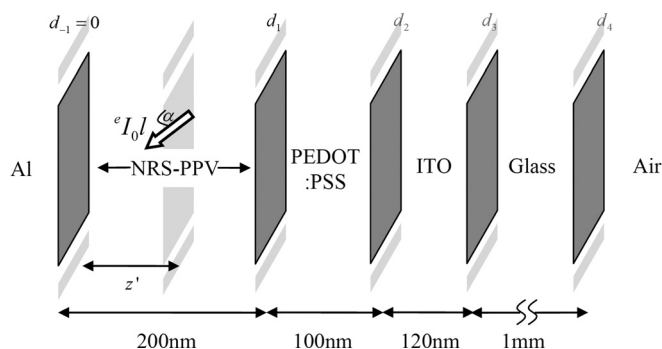


FIG. 2. Physical configuration of the prototype device, based on the device fabricated, characterized, and analyzed by Van Mensfoort *et al.*¹⁹ (Subsection III A).

asymmetrical emission zones with varying mean positions and widths, following Eqs. (10) and (15). For symmetrical EZ profiles, we have considered six EZ mean positions $\langle z' \rangle$, namely, 60 nm, 80 nm, 100 nm, 120 nm, 140 nm, and 160 nm, in conjunction with three EZ widths W , namely, 2 nm, 10 nm, and 20 nm, corresponding, altogether, to 18 different EZ profiles. The symmetrical effective spatial distribution is defined as

$$\bar{f}_{\text{sym}}^{\parallel}(z', \omega) = \frac{1}{F_{\text{sym}}} \exp\left\{-\frac{|z' - \langle z' \rangle|}{(W/2)}\right\}. \quad (28)$$

For the asymmetrical distributions, we have considered nine EZ profiles, exponentially decaying from the vicinity of the anodic facet of the active layer towards the cathode,^{18,42,44} with combinations of varying mean positions of $\langle z' \rangle = 140$ nm, 160 nm, and 180 nm, and varying widths of $W = 2$ nm, 10 nm, and 20 nm. The asymmetrical (left-decaying) effective spatial distribution is consequently defined for $z' \leq W + \langle z' \rangle$ as

$$\bar{f}_{\text{asym}}^{\parallel}(z', \omega) = \frac{1}{F_{\text{asym}}} \exp\left\{-\frac{W + \langle z' \rangle - z'}{W}\right\}, \quad (29)$$

and we note that the asymmetrical distribution peaks at $z' = W + \langle z' \rangle$, as opposed to the symmetrical distribution which peaks at $z' = \langle z' \rangle$. In both cases, provided the active layer is wide enough $d \gg W$, the distribution expectation value and standard deviation are $\langle z' \rangle$ and W , respectively (Fig. 3), and the parameter F is a normalization factor ensuring that $\int_0^d dz' \bar{f}^{\parallel}(z', \omega) = 1$.

As our method yields estimations using individual spectrally resolved emission patterns, i.e., it does not rely on any relations between different spectral components of the emission, we may disregard the spectral dependence of the prefactors $p(\omega)\bar{\eta}_{\text{ext}}^{\parallel}(\omega)$ in Eq. (15) for the simulation purposes. We have simulated emission in the spectral interval $\lambda \in [400 \text{ nm}, 800 \text{ nm}]$ in 5 nm steps and angular interval $\theta \in [-85^\circ, 85^\circ]$ in 1° steps. No artificial noise was added to the simulated data. The generated emission patterns were then used as input to a software tool⁴⁵ that we have developed, which implements the three steps of our analytical estimation method (Table I). Detailed description of the processing steps implemented by this software tool is enclosed in Appendix D.

Figures 4(a)–4(c) present representative simulated TE-polarized spectrally resolved emission patterns for three different symmetrical EZ profiles, sharing the same width $W = 10$ nm and differ in their mean position $\langle z' \rangle$. The output of the first step of the estimation procedure (Table I/step 1), namely, isolation of the image-source interference term (Eq. (12)) and identification of the extrema angles, is presented in Figs. 4(d)–4(f) as well. The black markers in Figs. 4(d) and 4(e) indicate positions of local maxima, as were identified by the software tool. Similarly, the white markers in Figs. 4(e) and 4(f) indicate local minima.

Figures 4(d)–4(f) indicate two important qualitative differences between IS interference patterns of EZs with different source-cathode separations,⁹ namely, the different spectral regions in which the local extrema appear, and their

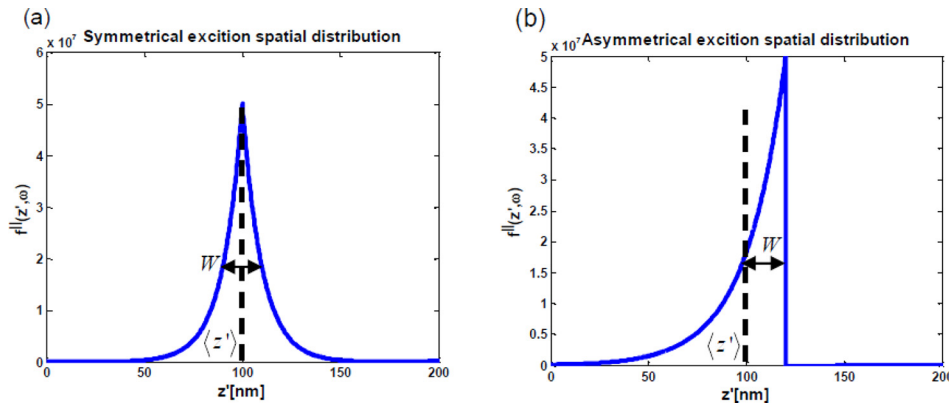


FIG. 3. Visual demonstration of the definitions of symmetrical (a) and asymmetrical (left-decaying) (b) spatial distribution functions, with expectation value and standard deviation $\langle z' \rangle = 100$ nm (dashed black line) and $W = 20$ nm (double sided arrow), respectively.

type (minimum or maximum); the implications of these observations on the estimation procedure will be addressed in detail in Subsections III A 1 and III A 2.

1. Symmetrical emission zone profiles: Mean position evaluation

Figure 5 presents the emission zone mean positions evaluated via Eq. (23) (Table I/step 2) from local minima (Fig. 5(c)) and local maxima (Fig. 5(d)), retrieved from data simulated for the symmetrical distributions defined in Eq. (28) (Fig. 3(a)). The extracted minima (Fig. 5(a)) and maxima (Fig. 5(b)) angles on which the estimation relies are also presented for reference (compare to Figs. 4(d)–4(f)).

To emphasize the simplicity of our method, we demonstrate the estimation of EZ mean position (Table I/step 2) for

the local minimum observed in the simulated IS interference pattern corresponding to $\langle z' \rangle = 120$ nm and $W = 10$ nm, received at $\theta_{\min} = 30^\circ$ for $\lambda = 490$ nm (marked by a red hexagon in Figs. 5(a) and 5(c) and in Fig. 4(e)). At this wavelength, the refractive index of the NRS-PPV active layer¹⁹ is $n_1 = 1.92$ and the extinction coefficient of the Aluminium cathode⁴³ is $\kappa_{-2} = 5.96$, which translates into $r_{\text{img}} = n_1/\kappa_{-2} = 0.322$ and $k_1 = 2\pi n_1/\lambda = 0.0246 \text{ nm}^{-1}$. For $\theta_{\min} = 30^\circ$, one gets $\chi_{\text{act}} = 0.97$, which yields $\alpha_{\text{img}} = |\angle \hat{\Gamma}_{-1}| = 0.5824$ radians. Substituting everything back to Eq. (23) using the condition for local minima and $\nu = 0$, yields $\langle z' \rangle = 119.76$ nm, which is the value marked by a red hexagon in Fig. 5(c). Note that this simple back-of-an-envelope calculation yields very accurate evaluation compared with the mean position of the simulated emission zone $\langle z' \rangle = 120$ nm. Carrying out this calculation iteratively for all identified local extrema of

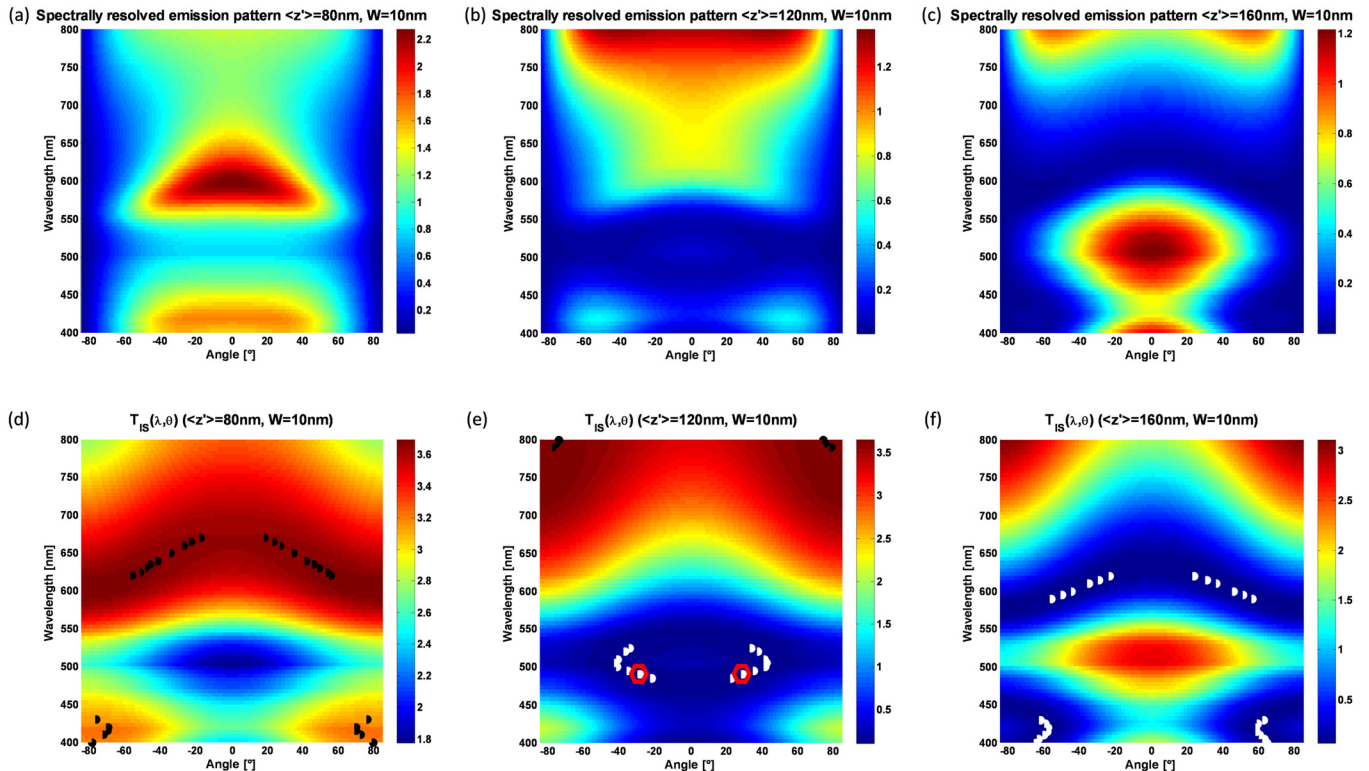


FIG. 4. Representative TE-polarized spectrally resolved emission patterns [(a)–(c)], simulated following Eq. (10), and the respective image-source interference patterns [(d)–(f)], extracted via Eq. (12) for the prototype device (Fig. 2). The presented patterns correspond to three different symmetrical emission zone profiles with constant width $W = 10$ nm and varying mean positions: (a) and (d) $\langle z' \rangle = 80$ nm; (b) and (e) $\langle z' \rangle = 120$ nm; (c) and (f) $\langle z' \rangle = 160$ nm. For the IS interference patterns (d)–(f), black and white markers indicate position of local maxima and minima, respectively, as identified by the software tool implementing the presented evaluation algorithm.⁴⁵ A red hexagon marks the local minimum at $\theta_{\min} = 30^\circ$ and $\lambda = 490$ nm in (e).

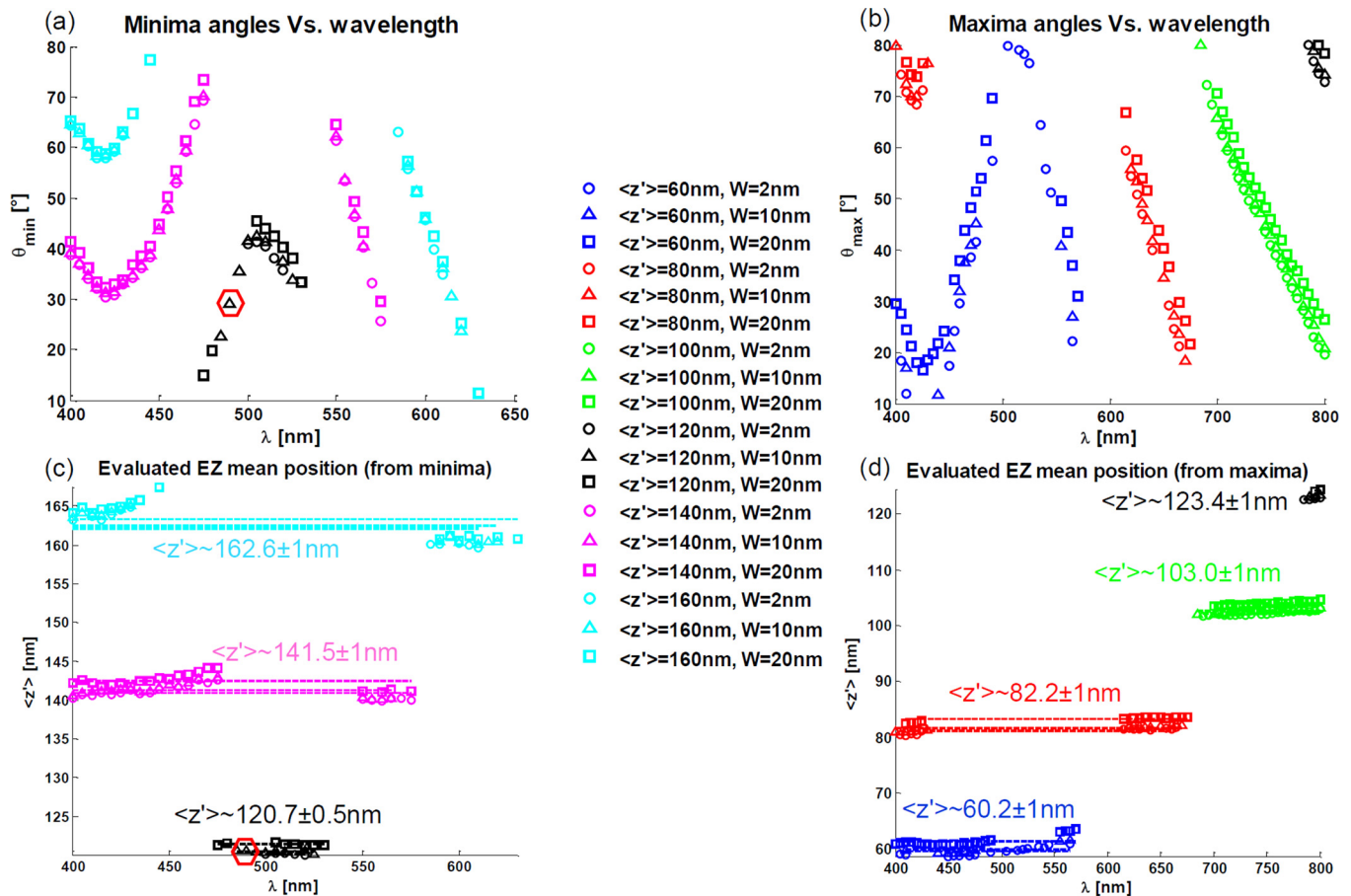


FIG. 5. Evaluation of emission zone mean position from simulated emission pattern image-source interference extrema, corresponding to the device described in Subsection III A hosting symmetrical EZ profiles. Six EZ mean positions $\langle z' \rangle$ are considered, namely, 60 nm (blue), 80 nm (red), 100 nm (green), 120 nm (black), 140 nm (magenta), and 160 nm (cyan), in conjunction with three EZ widths W , namely, 2 nm (circles), 10 nm (triangles), and 20 nm (squares), corresponding, altogether, to 18 different EZ profiles. The generated emission patterns were simulated in the spectral interval $\lambda \in [400 \text{ nm}, 800 \text{ nm}]$ in 5 nm steps. We present the extracted IS interference minima (a) and maxima (b) angles, and the EZ mean position as evaluated from these minima (c) and maxima (d) angles, as a function of wavelength and EZ profile. Averaged values for each EZ profile appear in dashed lines, along with the corresponding mean evaluated $\langle z' \rangle$ of all EZ profiles with the same mean position (and varying widths); the deviation is also indicated. Red hexagons mark the local minimum at $\theta_{\min} = 30^\circ$ and $\lambda = 490 \text{ nm}$ in (a) and (c).

Figs. 5(a) and 5(b) yields the results summarized in Figs. 5(c) and 5(d).

As expected from the nature of the IS interference phenomenon that is in the basis of the evaluation procedure, different source-cathode separations (i.e., different EZ mean positions) produce distinct extrema in different spectral regions (Figs. 5(a) and 5(b)); also, the type of extrema (minima or maxima) varies with this parameter (see also Figs. 4(d)–4(f)). Nonetheless, by considering the whole $\lambda \in [400 \text{ nm}, 800 \text{ nm}]$ spectral range we have achieved an accurate evaluation of the EZ mean position for all EZ profiles considered, with uncertainties below 5 nm.

Of course, standard OLEDs do not usually emit well throughout a 400 nm spectral width. However, the results in Figs. 5(a)–5(d) do not imply it is essential to utilize the *complete* visible spectrum for the evaluation procedure, but rather that for different emission zone mean positions, *different* regions of the emission spectrum yield proper estimations of this parameter. Hence, our method could probably be applied to typical OLEDs without taking special design measures to facilitate EZ evaluation (cf. Ref. 20, Sec. 4) if the measurements extend over the entire available emission

spectrum (recall that we require only a single appropriate monochromatic emission pattern to produce an estimation). Even if the relevant spectral regions are located at the tails of the EL spectrum (which is usually the case in optimized OLEDs²⁰), our algorithm may be applied successfully, due to the fact that local extrema form a very distinct feature of interference patterns, and can be accurately evaluated even for low signal-to-noise ratios; this will be demonstrated in Subsection III B for experimental data.

In consistency with our methodology, which treats the spectral broadening as a perturbation (Sec. II/Assumption 3), the results for the prototype device indicate that indeed the mean position of the emission zone is quite decoupled from its width, and the extrema angles (Figs. 5(a) and 5(b)) and consequently the evaluated mean positions (Figs. 5(c) and 5(d)) are not very sensitive to this parameter.

2. Symmetrical emission zone profiles: Width evaluation

Figure 6 presents the emission zone widths evaluated via Eq. (26) (Table I/step 3) from the simulated IS

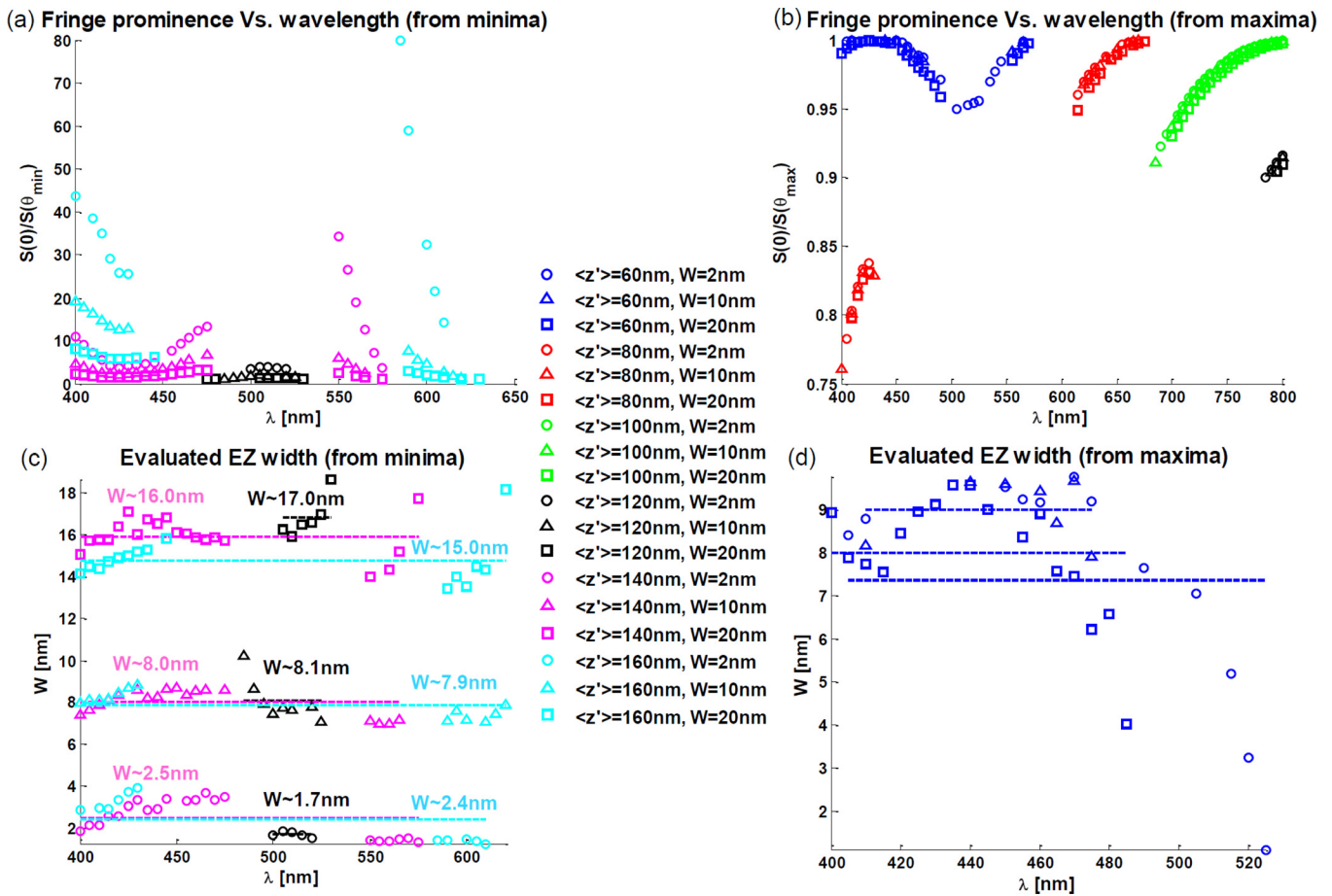


FIG. 6. Evaluation of emission zone width from simulated emission pattern image-source interference fringe prominence, corresponding to the device described in Subsection III A hosting symmetrical EZ profiles. The legend is as in Fig. 5. We present the extracted IS interference fringe prominence for the minima (a) and maxima (b) angles presented in Figs. 5(a) and 5(b), and the EZ widths as evaluated from these minima (c) and maxima (d) angles, as a function of wavelength and EZ profile. Averaged values for each EZ profile appear in dashed lines, along with the corresponding mean evaluated W for each EZ profile.

interference fringe prominence, corresponding to the local minima (Fig. 6(c)) and local maxima (Fig. 6(d)) presented in Figs. 5(a) and 5(b). The ratios between the forward emission and the minima (Fig. 6(a)) or maxima (Fig. 6(b)) side lobe emission on which the estimation relies are also presented for reference.

Examination of Figs. 6(a) and 6(b) reveals an important difference between the fringe prominence calculated from destructive (minima related) and constructive (maxima related) image-source interference. Whereas the fringe prominence computed from destructive side lobes (Fig. 6(a)) exhibits a large dynamical range, with significant differences between values corresponding to different EZ widths, the fringe prominence values computed from constructive side emission (Fig. 6(b)) are practically insensitive to variations in EZ width. This explains why the estimation procedure works rather well for emission zones for which the IS interference produces distinct minima (e.g., $\langle z' \rangle = 120$ nm, 140 nm, 160 nm, see Fig. 6(c)), while resulting in a complete failure for emission zones which only produces interference maxima (e.g., $\langle z' \rangle = 60$ nm, 80 nm, 100 nm, see Fig. 6(d)). In fact, for EZ profiles with $\langle z' \rangle = 80$ nm and $\langle z' \rangle = 100$ nm we do not even get a valid evaluation (i.e., there is no real solution to Eq. (26)). This suggests that in order to achieve accurate evaluation of EZ widths, the OLED under

test should operate in conditions which produce IS interference minima in a given spectral range, and these should be used for the evaluation procedure (see also Flämmich *et al.*,²⁰ cf. Figs. 2 and 3 therein). We emphasize that while this sensitivity issue has a large impact on the EZ width evaluation, EZ mean position can be still accurately evaluated from emission patterns containing only local maxima, as discussed in Subsection III A 1.

It is worth noting that the slight underestimation of the EZ widths for broad emission zones ($W = 10$ nm and $W = 20$ nm) originates in the approximated moment representation of Eq. (17) (Sec. II/Assumption 3). This may be improved by choosing different forms of approximation (e.g., the Padé approximant) in case some knowledge on the expected shape of the emission zone is available *a priori*.

3. Asymmetrical emission zone profiles

We now turn to examine the sensitivity of our evaluation procedure to the exact shape of the spatial distribution. To that end, we employ our method on simulated emission patterns produced for the prototype device hosting asymmetrical (left-decaying) emission zones, as defined in Eq. (29) (Fig. 3(b)). Figure 7 presents the mean position (Fig. 7(a)) and width (Fig. 7(b)) evaluated from the simulated IS

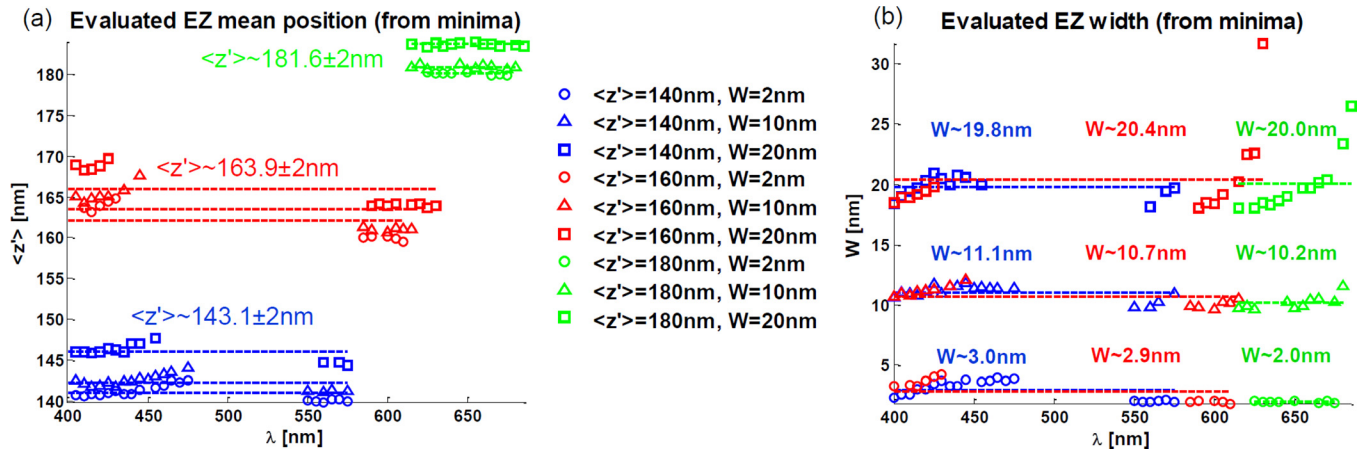


FIG. 7. Evaluation of emission zone mean position (a) and width (b) from simulated emission pattern image-source interference fringe angles and prominence, corresponding to the device described in Subsection III A hosting asymmetrical EZ profiles. Three EZ mean positions (z') are considered, namely, 140 nm (blue), 160 nm (red), and 180 nm (green), in conjunction with three EZ widths W , namely, 2 nm (circles), 10 nm (triangles), and 20 nm (squares), corresponding, altogether, to nine different EZ profiles. (a) Averaged values for each EZ profile appear in dashed lines, along with the corresponding mean evaluated (z') of all EZ profiles with the same mean position (and varying widths); the deviation is also indicated. (b) Averaged values for each EZ profile appear in dashed lines, along with the corresponding mean evaluated W for each EZ profile.

interference local minima and the corresponding fringe prominence values. The results clearly indicate that the evaluation procedure performs well also for asymmetrical distributions, with accuracies comparable to those received for symmetrical distributions with the same mean position and width (Figs. 5(c) and 6(c)), despite the significant differences in the full moment series expansion of the two types of distributions.⁹

The disregard of high order moments Eq. (17) (Sec. II/Assumption 3) does result in an overestimation of the EZ mean position as the EZ width becomes larger (Fig. 7(a)); however, this drift does not deteriorate significantly the accuracy of the results, which remains better than 5% for EZ mean position. As with the symmetrical distributions, applying the estimation method on data related to maxima angles yields reasonable estimation of the EZ mean position, however, fails to recover the EZ width due to the limited dynamical range of the fringe prominence values (not shown).

This verifies the robustness of our method, yielding accurate estimations of the EZ mean position and width for these two prototypical spatial distribution functions; thus, we expect the method to perform well also for arbitrary EZ profiles.

B. Application of the method on experimental data

After verifying our method in a controlled manner on data sets simulated for a prototype device, we apply it to experimental data measured for a blue polymer OLED (P-OLED) designed, fabricated, and characterized by Roberts *et al.*⁴⁴ The P-OLED consists of an Aluminium cathode, a 130 nm thick light-emitting polymer (LEP) layer, a 15 nm thick IL, a 35 nm thick hole injection layer (HIL), a 45 nm thick ITO anode, and a 0.7 mm thick glass substrate (Fig. 8). TE-polarized and TM-polarized spectrally resolved emission patterns were measured using an index matched glass hemisphere attached to the bottom of the substrate, which extends the angular content of the outcoupled emission (see note on the last paragraph of Appendix A).

The emission was measured for wavelengths in the range $\lambda \in [360 \text{ nm}, 830 \text{ nm}]$ in 10 nm steps, and angles in the range $\theta \in [-70^\circ, 70^\circ]$ in 10° steps. As discussed in Appendix D, our software tool⁴⁵ interpolates these data to facilitate higher accuracy of extrema extraction, estimating the emission over a finer grid of 5 nm spectral steps and 1° angular steps. Nonetheless, when presenting the results of the estimation method in this subsection, we limit ourselves to the measured angular interval and the set of wavelengths in which emission patterns were actually measured; this ensures the reliability of the error analysis.

Complete details regarding the device properties and characterization techniques can be found in Ref. 44. The relative error in intensity measurement is estimated to be limited by 5% from comparison between emission values measured at corresponding positive and negative angles, which should be identical due to symmetry considerations; a similar limit is assessed from deviations between repeated measurements (not shown).

Figure 9 presents the measured TE-polarized spectrally resolved emission patterns (Figs. 9(a)–9(c)) and the respective image-source interference patterns computed via Eq. (12) (Figs. 9(d)–9(f)), for three different operating

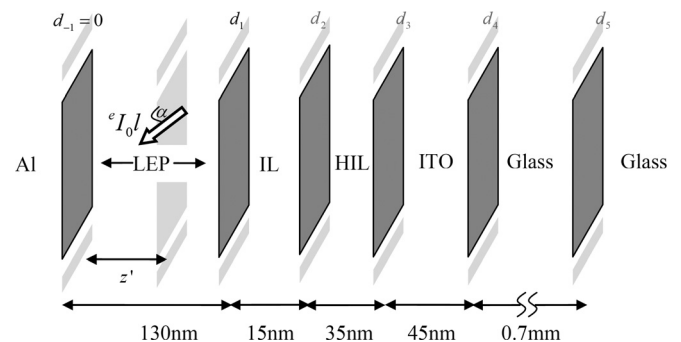


FIG. 8. Physical configuration of the blue polymer OLED fabricated, characterized, and analyzed by Roberts *et al.*⁴⁴ (Subsection III B).

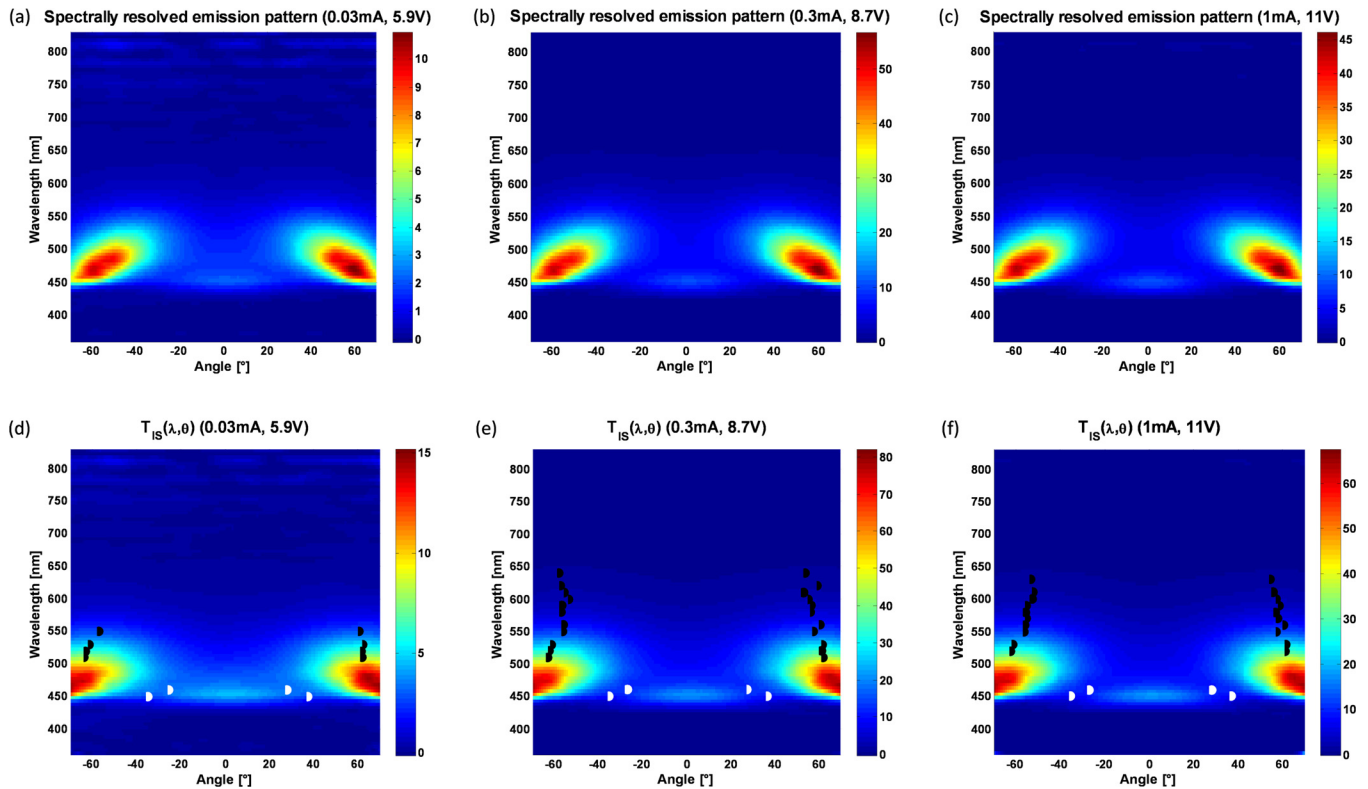


FIG. 9. Measured TE-polarized spectrally resolved emission patterns [(a)–(c)] and the respective image-source interference patterns [(d)–(f)] of the P-OLED designed, fabricated, and characterized by Roberts *et al.*⁴⁴ (Subsection III B). Measurements were performed for three different operating conditions: (a) and (d) low current (0.03 mA, 5.9 V); (b) and (e) medium current (0.3 mA, 8.7 V); (c) and (f) high current (1 mA, 11 V).

conditions: low current (0.03 mA, 5.9 V) (Figs. 9(a) and 9(d)), medium current (0.3 mA, 8.7 V) (Figs. 9(b) and 9(e)), and high current (1 mA, 11 V) (Figs. 9(c) and 9(f)).

The distribution of the identified local extrema marked in Figs. 9(d)–9(f) provides another support to the conclusions presented in Subsection III A 1. As was observed therein for simulated data, local extrema of the experimental patterns are also found in a rather wide spectral range, including regions far away from the central EL wavelength.⁴⁴ This implies once again that if the entire available emission spectrum is considered, recovering emission zone properties of OLEDs may be realized without the necessity to specially design them.

Figure 10 presents the estimated values of EZ mean position (Figs. 10(a) and 10(b)) and width (Figs. 10(c) and 10(d)) evaluated from minima (Figs. 10(a) and 10(c)) and maxima (Figs. 10(b) and 10(d)) extracted from Figs. 9(d)–9(f) following our method. However the scatter of the evaluated EZ mean positions is greater than obtained for the simulated emission patterns, it is clear that the excitons form preferably far from the cathode/organic interface of the 130 nm thick active layer, quite close to the LEP/IL interface, with mean exciton-cathode separations in the range of 100–130 nm (Figs. 10(a) and 10(b)). This would usually indicate that the electron and hole mobilities (μ_e and μ_h , respectively) are imbalanced, with the high mobility electrons injected from the cathode flowing in the device faster than the low mobility holes injected from the anode facet, causing the formation of the excitons rather far away from the cathode ($\mu_e^{\text{LEP}} > \mu_h^{\text{LEP}}$).

In addition, if we account for the fact that our investigations so far (Subsection III A) have shown that EZ widths

evaluated from IS interference minima are more reliable, we may conclude, by analyzing Figs. 10(a) and 10(c), that subtle but consistent differences in the way excitons are formed in each one of the current regimes exist; this is despite the fact that it is hard to notice any significant differences between the plots in Figs. 9(d)–9(f) by a mere visual inspection. The estimated values imply that while the EZ mean position remains more or less the same for all operating conditions, the EZ width is consistently reduced for increasing applied current and electric field, from $W \sim 26.2 \pm 3$ nm (low current), via $W \sim 19.4 \pm 1$ nm (medium current), to $W \sim 17.0 \pm 1$ nm (high current); the same trend is observed for the values estimated for each spectral line individually. This observation supports the hypothesis that in the measured device electron mobilities are larger than hole mobilities, as in such a scenario, increase in the external voltage affects electron velocities more than it affects hole velocities, causing the excitons to form closer to the LEP/IL interface.

1. Construction of the estimated emission zone profile

As implied by the formulation in Sec. II, our method provides information regarding the first two moments of the EZ profile, $\langle z' \rangle$ and W ; however, it does not indicate what is the exact functional dependence that describes that profile. In order to construct an equivalent exciton distribution, one must use the physical characteristics of the device in conjunction with the evaluated properties. We demonstrate such a construction procedure using the P-OLED investigated in this subsection. As the estimated values of the EZ mean positions and widths presented in Fig. 10 indicate that

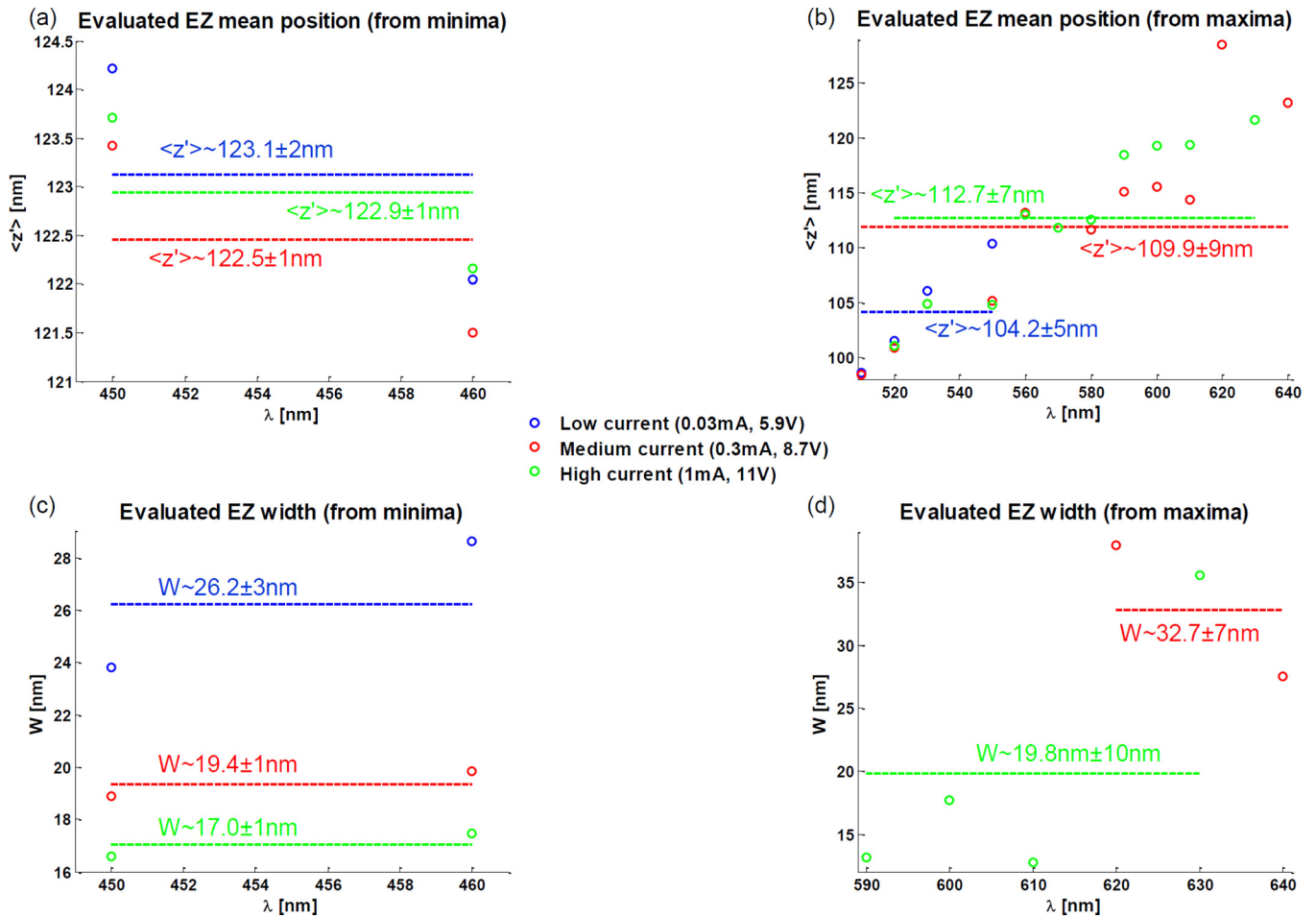


FIG. 10. Evaluation of emission zone mean position [(a) and (b)] and width [(c) and (d)] from measured emission pattern image-source interference minima [(a) and (c)] and maxima [(b) and (d)] and respective fringe prominence, corresponding to the P-OLED device designed, fabricated, and characterized by Roberts *et al.*⁴⁴ (Subsection III B). The raw emission patterns, presented in Fig. 9, were collected in three different operating conditions: low current (0.03 mA, 5.9 V) (blue), medium current (0.3 mA, 8.7 V) (red), and high current (1 mA, 11 V) (green). Averaged values for each current regime appear in dashed lines, along with the corresponding mean evaluated $\langle z' \rangle$ [(a) and (b)] and W [(c) and (d)]; the standard deviation is also indicated.

$\mu_e^{\text{LEP}} > \mu_h^{\text{LEP}}$, it would be reasonable to use an asymmetrical left-decaying exponential distribution to describe the effective spatial distribution of the excitons.^{18,42,44} Using the definition in Eq. (29), we may construct such a distribution function for each pair of evaluated $\langle z' \rangle$ and W from Figs. 10(a) and 10(c) and then average the resultant profiles.

Figure 11 presents the evaluated effective spatial distribution resulting from such a procedure. The narrowing phenomenon attributed to the mobility imbalance is indeed observed for increasing current conditions. However, the profiles indicate that a significant fraction of the excitons resides in the IL, and these are the ones responsible for most of the aforementioned narrowing.

Indeed, both LEP and IL of the measured P-OLED contain fluorescent molecular sites.⁴⁴ Moreover, the electrical characterization conducted by Roberts *et al.*⁴⁴ implies that in the IL the holes are those which have the higher mobility. More specifically, they conclude therein that $\mu_h^{\text{IL}} > \mu_e^{\text{LEP}} > \mu_e^{\text{IL}} > \mu_h^{\text{LEP}}$. Therefore, a more appropriate model for the effective spatial distribution function would be an asymmetrical bilateral exponential function, which peaks at the LEP/IL interface and decays with widths W_- and W_+ to the left and to the right of this interface, respectively (Fig. 5 of Ref. 44).

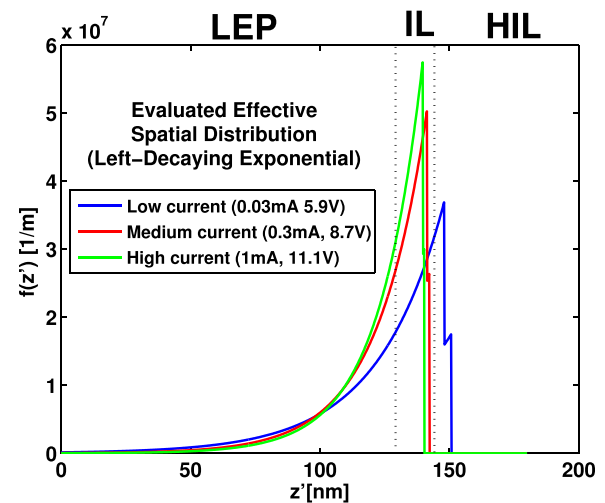


FIG. 11. Evaluated effective spatial distribution functions, based on estimated EZ mean positions and widths presented in Figs. 10(a) and 10(c) for the P-OLED measured by Roberts *et al.*,⁴⁴ using the left-decaying exponential model. The three EZ profiles correspond to the low (blue), medium (red), and high (green) current regimes. Two dotted lines indicate the positions of the LEP/IL and IL/HIL interfaces.

Given the estimated values of the EZ mean position $\langle z' \rangle$ and width W , and the desirable position of its peak d , such a bilateral exponential function may be defined as follows:

$$\bar{f}_{\text{bi}}^{\parallel}(z', \omega) = \frac{1}{F_{\text{bi}}} \begin{cases} \exp\left\{-\frac{|d-z'|}{W_-}\right\} & z' \leq d \\ \exp\left\{-\frac{|d-z'|}{W_+}\right\} & z' > d, \end{cases} \quad (30)$$

where

$$W_{\pm} = \frac{1}{2} \left[\pm(\langle z' \rangle - d) + \sqrt{2W^2 - (\langle z' \rangle - d)^2} \right].$$

These definitions ensure that provided the LEP and IL are wide enough, the mean and standard deviation of this function would be $\langle z' \rangle$ and W , respectively.

Figure 12 presents the EZ profiles evaluated based on this bilateral exponential model. With respect to Fig. 11, the narrowing is now more symmetrical, in consistency with the mobility imbalance in the various layers measured by other means.⁴⁴ While in principle both models can describe well the emission zone characteristics of the device, the electrical discontinuity at the LEP/IL interface implies that the EZ profiles constructed based on the bilateral exponential model are more probable from a physical perspective.

It should be noted at this stage that the results presented in this subsection agree very well with the EZ properties obtained by numerical fitting techniques for the same device, presented by Roberts *et al.*⁴⁴ (see Subsection 3.5 therein) and verified by other means as well, e.g., electrical simulations and measurements. In particular, the EZ width W was numerically estimated there to be 25 nm, 20 nm, and 16 nm, for the low, medium, and high current operating conditions (see squares in Fig. 12 of Ref. 44), which are in a very good agreement with the values extracted by our analytical method (Fig. 10(c)); good agreement is achieved for the EZ mean positions as well. These results indicate that the

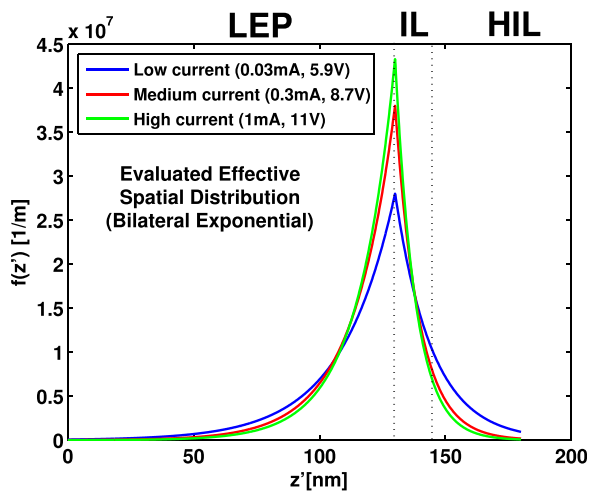


FIG. 12. Evaluated effective spatial distribution functions, based on estimated EZ mean positions and widths presented in Figs. 10(a) and 10(c) for the P-OLED measured by Roberts *et al.*,⁴⁴ using the asymmetrical bilateral exponential model. The legend is as in Fig. 11.

accuracy of the suggested analytical algorithm is comparable with that achieved by numerical methods, and that it may perform well when applied to experimental data.

2. Effect of external quantum efficiency

When the variation of the EZ mean positions evaluated from IS interference local maxima (Fig. 10(b)) is examined in more detail, it seems that there exists a consistent monotonic increase of the estimated values with increasing wavelength. This allegedly contradicts our previous observations (Subsection III A) that while inaccuracies in the EZ widths evaluated from maxima are expected, the evaluation of EZ mean positions from these angles should exhibit small uncertainties (see, for comparison, Fig. 5(d)). If we disregard possible inaccuracies originating from emission pattern or material dispersion measurement errors, we may relate this monotonic increase in EZ mean position to the dependence of the effective contribution of the HEDs to the EQE in dipole position and radiation frequency, as formulated in Eqs. (13) and (14).

As laid out by Eqs. (15)–(17), our evaluation procedure is capable of estimating the effective spatial HED distribution $\bar{f}^{\parallel}(z', \omega)$ of Eq. (14), which is a product of the spatial distribution of the excitons $f(z')$ and the relative EQE of the HEDs $\bar{\eta}_{\text{ext}}^{\parallel}(z', \omega)/\bar{\eta}_{\text{ext}}^{\parallel}(\omega)$, which is frequency dependent. In other words, the effective spatial distribution we estimate corresponds to the distribution of *efficiently* radiating excitons in each wavelength, indicating the zone from which the *observed* emission originates at that wavelength. Therefore, optical processes altering the molecular lifetime, e.g., weak-microcavity interference and cathode quenching effects, which are frequency-dependent, are expected to shift the weight of the evaluated effective distribution $\bar{f}^{\parallel}(z', \omega)$ towards the spatial regions which outcouple best at the frequency ω .

Complete decoupling between the actual exciton distribution $f(z')$ and the EQE effects requires knowledge of the orientation distribution of the dipoles, as well as consideration of the relations between emission patterns measured at different wavelengths (Eqs. (13) and (14)); these steps require numerical fitting of the data. Nonetheless, to examine the relations between the EQE effects and the trend observed in Fig. 10(b), a simplified procedure can be harnessed to estimate the relative EQE dependency in emitter position and frequency. This is achieved by assuming that the internal quantum efficiency does not vary much with dipole position and orientation; using an equivalent dipole orientation of $\alpha = 70^\circ$ (Ref. 44) for Eq. (13); and considering that most of the excitons are concentrated between $z' = 120$ nm and $z' = 130$ nm (Figs. 10(a)–10(c)) for normalizing Eq. (14).

Figure 13(a) presents the estimated relative EQE of Eq. (14) as a function of emitter-cathode separation and wavelength, for $z' \in [90$ nm, 130 nm] and $\lambda \in [510$ nm, 640 nm]. It is readily observed that while the dependency of the relative EQE in z' is rather small for $\lambda \approx 640$ nm, as the wavelength decreases emissive sites away from the anode ($z' \rightarrow 90$ nm) become more efficient with respect to those closer to it ($z' \rightarrow 130$ nm). This dependency of $\bar{\eta}_{\text{ext}}^{\parallel}(z', \omega)/\bar{\eta}_{\text{ext}}^{\parallel}(\omega)$ in

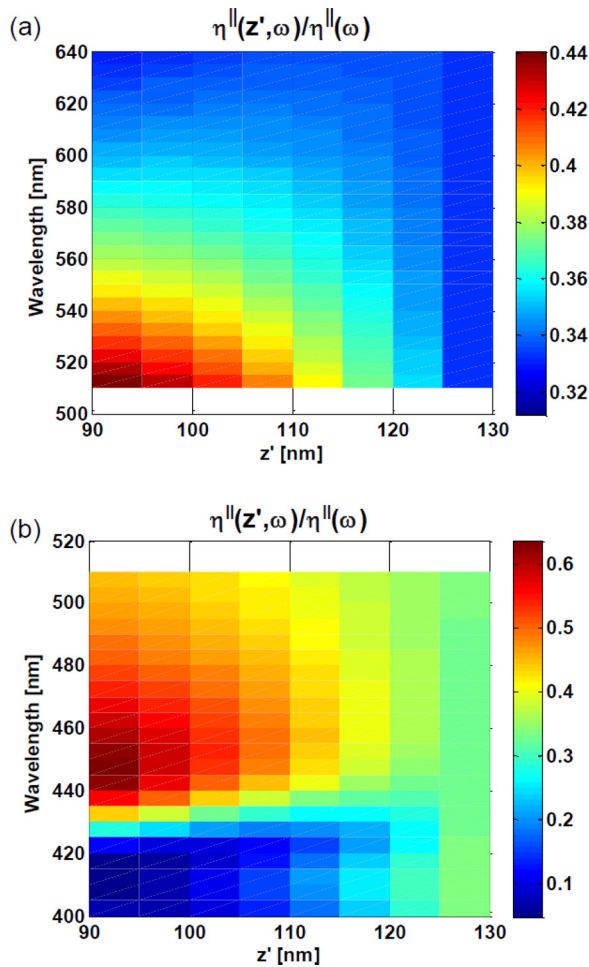


FIG. 13. Relative effective contribution of the HEDs to the EQE $\bar{\eta}_{\text{ext}}^{\parallel}(z', \omega)/\bar{\eta}_{\text{ext}}^{\parallel}(\omega)$ calculated via Eqs. (13) and (14) and the simplified procedure outlined in the text, for emitter-cathode separations in the range $z' \in [90 \text{ nm}, 130 \text{ nm}]$ and emission wavelength in the ranges (a) $\lambda \in [510 \text{ nm}, 640 \text{ nm}]$ and (b) $\lambda \in [400 \text{ nm}, 510 \text{ nm}]$ (note the different color bar).

conjunction with Eq. (14) has two important implications: first, it implies that the evaluated effective distribution $\bar{f}^{\parallel}(z', \omega)$ at $\lambda \approx 640 \text{ nm}$, where the relative EQE is rather indifferent to the emitter location, is a good approximation for the actual exciton distribution $f(z')$; second, it implies that as the wavelength gets shorter, the mean position of $\bar{f}^{\parallel}(z', \omega)$ is expected to shift toward shorter emitter-cathode separation distances. These two conclusions are in a very good agreement with the mean position values estimated from local maxima (Fig. 10(b)).

We attempt to apply the same argumentation to the EZ mean positions estimated from local minima (Fig. 10(a)); Fig. 13(b) presents the relative EQE for the relevant spectral range $\lambda \in [400 \text{ nm}, 510 \text{ nm}]$ (note the different color bar). The plot reveals that due to the frequency dependence of interference effects within the OLED weak-microcavity, the relative EQE trend flips when the wavelength approaches $\lambda \approx 430 \text{ nm}$, and the efficient emitter positions appear adjacent to the anode again; this is consistent with the estimations in Fig. 10(a) evaluated at $\lambda \in [450 \text{ nm}, 460 \text{ nm}]$. Although the change in relative EQE trend appears to happen at slightly longer wavelengths than predicted by Fig. 13(b), the two results are in a qualitative agreement, providing

another support to our interpretation of the variation of evaluated EZ mean positions with wavelength.

As a final note, although this coupling between the actual exciton distribution and the relative EQE introduces an uncertainty to the evaluated profile $f(z')$, the deviation of EZ mean position due to this effect is limited by the EZ width. Therefore, we may avoid a detailed analysis of the relative EQE effects as conducted in this subsection, and approximate $f(z')$ by averaging the resultant $\bar{f}^{\parallel}(z', \omega)$ at various frequencies, without significantly deteriorating the estimation accuracy.

IV. CONCLUSION

In conclusion, we have presented a rigorous derivation of closed-form analytical relations between the constituent characteristics of the effective exciton spatial distribution in OLEDs, and the main features of the image-source interference fringes, which may be retrieved from measured emission patterns. The formulation results reveal that Bragg's condition can be used to evaluate the emission zone mean position and width, respectively, from the angles of constructive and destructive interference, and the respective fringe prominence. The method was verified using controlled simulated emission patterns, and employed successfully on experimental data, exhibiting good agreement with the results of numerical techniques.

Our investigation suggests that due to differences in the dynamical range of fringe prominence values for emission patterns exhibiting distinct minima or maxima, evaluation of EZ width from local minima is more reliable; extraction of EZ mean position seems to perform equally well for IS interference minima and maxima. We have demonstrated that our method yields accurate results for a wide range of source-cathode separations without resorting to specially designed OLEDs, provided that a wide spectral range is included in the measurements. The interpretation of the estimated exciton distribution in the context of construction of the EZ profile and the effects of the EQE frequency dependency was discussed in detail and demonstrated using experimental data.

Although following an analytical approach introduces inevitable approximations to the final results, the computational simplicity and physical clarity provided by our method make it very appealing for preliminary design or production-line verification, which usually do not require very high accuracy. Moreover, the successful demonstrations presented herein indicate that the assumptions our procedure relies on are valid for many typical devices. Therefore, the method introduced herein forms an efficient engineering tool, which complements the numerical techniques exclusively solving the emission zone problem to date.

ACKNOWLEDGMENTS

This research was partially supported by the Ollendorff Minerva Center and by the Israeli Nanotechnology Focal Technology Area on "Nanophotonics for Detection." A.E. gratefully acknowledges the support of The Clore Israel Foundation Scholars Programme. The authors also wish to thank the reviewers for their detailed and constructive comments.

APPENDIX A: OLEDS WITH LAYERS THICKER THAN THE ENSEMBLE COHERENCE LENGTH

For layers thicker than the coherence length defined by the emission bandwidth or the spectral resolution of the measurements, $L_c = c/\Delta\omega$, Eq. (4) would produce spurious weak-microcavity interference fringes which would not be observable in measured data.^{9,37,46} In more detail, if an interference process takes place between rays multiply-reflected between two boundaries at $z = d_{n_1}$ and $z = d_{n_2}$, the distance between which satisfying $|d_{n_1} - d_{n_2}| \gg L_c$, then within the spectral range of the source ensemble there would be an infinitely large number of frequencies that would yield constructive interference and an equally large number of frequencies that would yield destructive interference, for a given observation angle. Thus, when the integrated spectral response of the ensemble is considered, the interference cross-terms related to this process would be highly attenuated, and may be neglected for any practical matters.^{9,37,47} On the other hand, if the cavity thickness satisfies $|d_{n_1} - d_{n_2}| \ll L_c$, then the interference cross-terms are unaffected by the spectral broadening.

The coherence length relevant to our discussion is given by³⁷ $L_c = \max\{L_{c,\text{ens}}, L_{c,\text{meas}}\}$, where the ensemble coherence length $L_{c,\text{ens}} = c/\Delta\omega$ is inversely proportional to the source spectral width $\Delta\omega$, and the spectral resolution of the measurement $\Delta\lambda_{\text{meas}}$ (in wavelength units) dictates the measurement coherence length $L_{c,\text{meas}} = \lambda^2/(2\pi\Delta\lambda_{\text{meas}})$. In typical OLEDs, the coherence length of the ensemble is of the order of $L_{c,\text{ens}} \sim 3 \mu\text{m} - 20 \mu\text{m}$,⁴⁸ while a typical measurement resolution of $\Delta\lambda_{\text{meas}} = 1 \text{ nm}$ dictates $L_{c,\text{meas}} \sim 25 \mu\text{m} - 100 \mu\text{m}$ (for the visible spectrum $\lambda \in [400 \text{ nm}, 800 \text{ nm}]$). In any case, as the OLED organic stack is usually submicron thick and the substrate usually $\sim 1 \text{ mm}$ thick, only the weak cavity formed between the cathode/organic and substrate/air interfaces would be affected by this spectral broadening effect.⁹

The practical consequence of this observation is that the expression for the weak-microcavity contribution (Eq. (4)) should be modified as to neglect all interference cross-terms originating in multiple reflections between the substrate/air interface and the OLED organic stack and cathode. This is facilitated by separating the substrate/air interface from the WM factor of Eq. (4), similarly to Shcherbakov *et al.*,⁴⁶

$$T_{WM}(k_t) = \frac{1}{|1 - \widehat{\Gamma}_{-1}(k_t)\widetilde{R}_1(k_t)e^{-2j\beta_1(d_1-d_{-1})}|^2} \times \prod_{n=1}^{N-2} \frac{1}{|1 + \Gamma_n(k_t)\widetilde{R}_{n+1}(k_t)e^{-2j\beta_{n+1}(d_{n+1}-d_n)}|^2} \times \frac{1}{1 - |\Gamma_N(k_t)\widehat{R}_{N-1}(k_t)|^2}, \quad (\text{A1})$$

where the modified total reflection coefficients are defined as to disregard the substrate/air interface via the recursion base condition, namely,

$$\begin{cases} \widetilde{R}_n(k_t) = \frac{\Gamma_n(k_t) + \widetilde{R}_{n+1}(k_t)e^{-2j\beta_{n+1}(d_{n+1}-d_n)}}{1 + \Gamma_n(k_t)\widetilde{R}_{n+1}(k_t)e^{-2j\beta_{n+1}(d_{n+1}-d_n)}} \\ \widetilde{R}_N(k_t) = 0, \end{cases} \quad (\text{A2})$$

and we introduce the total reflection coefficients in the reversed direction for $n > 0$, considering the reflection from the OLED organic and cathode stack of waves reflected back (to the left) from the substrate/air interface,

$$\begin{cases} \widehat{R}_n(k_t) = \frac{\widehat{\Gamma}_n(k_t) + \widehat{R}_{n-1}(k_t)e^{-2j\beta_n(d_n-d_{n-1})}}{1 + \widehat{\Gamma}_n(k_t)\widehat{R}_{n-1}(k_t)e^{-2j\beta_n(d_n-d_{n-1})}} \\ \widehat{R}_1(k_t) = \frac{\widehat{\Gamma}_1(k_t) + \widehat{\Gamma}_{-1}(k_t)e^{-2j\beta_1(d_1-d_{-1})}}{1 + \widehat{\Gamma}_1(k_t)\widehat{\Gamma}_{-1}(k_t)e^{-2j\beta_1(d_1-d_{-1})}}, \end{cases} \quad (\text{A3})$$

and $\widehat{\Gamma}_n$ is defined via Eq. (7).

In case the optical measurements are performed using an index-matched half-sphere,^{19,44,49,50} the reflection from the substrate/air interface can be neglected for emission pattern calculations, and the formulae (2)–(5) remain valid, provided we replace the air layer with a semi-infinite substrate, extending to $z \rightarrow \infty$.

APPENDIX B: OLEDS WITH ORGANIC LAYERS BETWEEN THE CATHODE AND THE ACTIVE LAYER

In many cases, it is sufficient to consider an OLED structure such as the one depicted in Fig. 1, in which the cathode and the active layer are adjacent (Sec. II/Assumption 1).^{18–20,44} For more general scenarios, in which the active layer is separated from the cathode by another stack of $M - 1$ organic layers (i.e., positioned between layer (-1) and layer (-2) in Fig. 1), the model can be used without change as long as their optical properties do not deviate much from these of the active material; we then use an average refractive index to represent the optical constituents of the layer ± 1 , e.g., as in Ref. 49.

If a mean medium approximation for these organic layers is not applicable due to significant refractive index differences, the electromagnetic model should be modified such that the local reflection coefficient $\widehat{\Gamma}_{-1}$ in Eqs. (2), (4), (A1), and (A3) is replaced by the total reflection coefficient \widehat{R}_{-1} , taking into account all multiple reflections at interfaces situated to the left of the active layer (see Ref. 9 for its definition).

Subsequently replacing $\widehat{\Gamma}_{-1}$ with \widehat{R}_{-1} and noting that the emission zone mean position $\langle z' \rangle$ is defined as the distance to the left interface of the active layer $d_{-1} = 0$ would retain the validity of Eqs. (15)–(20); however, the approximations (21) and (22), which lead to the analytical form of the extremum condition (23), would not be strictly applicable. Nonetheless, an approximate Bragg condition similar to Eq. (23) may be derived, where $\alpha_{\text{img}} = |\angle \widehat{R}_{-1}|$. In principle, this approximate condition would be valid as long as the dominant reflection from the interfaces to the left of the active layer would still arise from the cathode/organic boundary, and the main influence of the stack would be limited to variation of the phase accumulated during propagation from the source to the cathode and back. Quantitative evaluation of this generalization is left for future work.

APPENDIX C: EVALUATION OF EFFECTIVE DIPOLE ORIENTATION

As mentioned in Sec. I, a thorough discussion in the evaluation of effective dipole orientation is beyond the scope of this paper. However, it is worthwhile to denote the steps that may be taken in order to estimate this parameter. Our concept for evaluating the effective dipole orientation relies on the fact that the VEDs do not emit to the forward direction due to their intrinsic radiation pattern (Eq. (8)).^{20,30,31} This implies that we may use the measured TM-polarized emission in the forward direction, together with the EZ profile estimated according to Subsection II B, as a means to predict the TM-polarized emission pattern that would have been produced by HEDs alone; the deviation from this prediction would indicate the relative contribution of VEDs.

Formally, we define the effective contribution of the VEDs to the EQE in analogy to Eq. (13),

$$\bar{\eta}_{\text{ext}}^{\perp}(z', \omega) = \int_0^{\pi/2} d\alpha h(\alpha) \sin \alpha \cos^2 \alpha \eta_{\text{ext}}(z', \alpha, \omega), \quad (\text{C1})$$

transforming the expression for the measured TM-polarized emission pattern of Eq. (11) into

$${}^M S_r(\theta; \omega) = p(\omega) \int_{d_{-1}}^{d_1} dz' \left[\bar{\eta}_{\text{ext}}^{\parallel}(\omega) \bar{f}^{\parallel}(z', \omega) {}^M S_r^{\parallel}(\theta; z', \omega) + \bar{\eta}_{\text{ext}}^{\perp}(\omega) \bar{f}^{\perp}(z', \omega) {}^M S_r^{\perp}(\theta; z', \omega) \right], \quad (\text{C2})$$

where we used the definition of the effective spatial VED distribution function

$$\bar{f}^{\perp}(z', \omega) = f(z') \bar{\eta}_{\text{ext}}^{\perp}(z', \omega) / \bar{\eta}_{\text{ext}}^{\perp}(\omega); \quad (\text{C3})$$

the normalization factor ensures $\int_0^d dz' \bar{f}^{\perp}(z', \omega) = 1$.

Using the moments of $\bar{f}^{\parallel}(z', \omega)$ recovered in Subsection II B and the measured emission at $\theta = 0$ we may estimate the product $p(\omega) \bar{\eta}_{\text{ext}}^{\parallel}(\omega) \bar{f}^{\parallel}(z', \omega)$ and subsequently, via Eqs. (1)–(4), the HED contribution to the TM-polarized emission pattern for all relevant angles. Subtracting this result from Eq. (C2) yields the emission pattern produced by the VED ensemble alone. Finally, the procedure formulated by Eqs. (12)–(27) can be repeated⁵¹ in an analogous manner for this isolated VED emission pattern to estimate $p(\omega) \bar{\eta}_{\text{ext}}^{\perp}(\omega) \bar{f}^{\perp}(z', \omega)$. The ratio between this parameter and $p(\omega) \bar{\eta}_{\text{ext}}^{\parallel}(\omega) \bar{f}^{\parallel}(z', \omega)$, which was already evaluated, yields exactly the ratio between the effective contributions of the VEDs and HEDs to the EQE (Eqs. (14) and (C3)), namely,

$$\frac{\bar{\eta}_{\text{ext}}^{\perp}(z', \omega)}{\bar{\eta}_{\text{ext}}^{\parallel}(z', \omega)} = \frac{\int_0^{\pi/2} d\alpha h(\alpha) \sin \alpha \cos^2 \alpha \eta_{\text{ext}}(z', \alpha, \omega)}{\int_0^{\pi/2} d\alpha h(\alpha) \sin^3 \alpha \eta_{\text{ext}}(z', \alpha, \omega)}, \quad (\text{C4})$$

which can be used to deduce the nature of the orientation distribution $h(\alpha)$.

APPENDIX D: EMISSION ZONE ESTIMATION SOFTWARE TOOL

For the sake of completeness, we provide herein details regarding the processing steps implemented by the software tool “Where Is My Emission Zone?++” (WIMEZPP), developed to apply the analytical EZ estimation algorithm described in this paper to simulated and experimental data.⁴⁵ The main routines in WIMEZPP employ the three steps of our method (Table I): isolation of the image-source interference term; identification of the extrema angles and evaluation of the emission zone mean position (Subsection II B 1); and retrieval of the fringe prominence and estimation of the emission zone width (Subsection II B 2).

To reduce noise-related issues, which may become critical when isolating the IS interference pattern (which requires a division of the input data by an analytical function, possibly obtaining small values), and to facilitate proper identification of local extrema, a pre-processing interpolation step is implemented. This step consists of a cubic polynomial interpolation of the input emission values between neighbouring spectral and angular grid points, which is provided, for instance, by the standard MATLAB procedure `fit(gridPoints, rawData, 'cubicinterp')`. After applying this step, the raw data are not represented by a set of sampled grid points anymore, but by a set of cubic polynomial coefficients, which are associated with each interval between two original grid points. In another words, the raw data is now a smooth function, which can be evaluated and differentiated in each desirable point with reduced noise-related problems. In addition, when obtaining this interpolation we demand that the emission would vanish as the observation angle goes to $\pm 90^\circ$, thus increasing the accuracy of local extrema identification near the limits of the measured angular interval, relying on physical rationale.

For our purposes, it is sufficient to interpolate the input data to match a 2D grid with spectral resolution of 5 nm and angular resolution of 1° . Nonetheless, when presenting the results of the estimation method (Subsection III B), we have limited ourselves to the specific measured wavelength values, and the measured angular interval; this ensures the reliability of the error analysis.

Although interpolation does not add any information content to the raw data *per se*, it serves as an important accessory tool to interpretation of the data, especially if automatic accurate detection of local extrema, such as required by WIMEZPP, is to be implemented. The reason for that is the fact that local extrema are a rather “global” property of a function, in terms of sampled grid points: in case a local extremum lies between two neighbouring grid points, it is important to know how to connect these points in order to achieve an accurate evaluation of extrema angles and emission. Using the physical constraints that the emission pattern must be smooth both with respect to angle variation and wavelength variation, and that emission must vanish as the

observation angle approaches the horizon, we are able to represent the raw data as a physically consistent smooth function and consequently evaluate these parameters accurately.

It is important to note that this pre-processing step is not essential if highly resolved measurements in the angular domain are available. Moreover, if the analytical estimation is applied “manually” on a single (monochromatic) emission pattern, plotting the IS interference pattern using a standard visual software tool such as MATLAB or Microsoft Excel is usually sufficient for an accurate evaluation of both local extremum angles and fringe prominence values *by inspection* (these tools usually plot interpolated data by default). An example to such a manual application can be found in Ref. 24, highly emphasizing the simplicity and efficiency of the proposed method.

Lastly, to ensure a physically consistent identification of local extrema in noisy experimental data, which is a critical step in our estimation method, we follow these rules

1. We restrict ourselves to local extrema found in the angular range $|\theta| \in [10^\circ, 80^\circ]$. At small observation angles $|\theta| < 10^\circ$, the dominant local extremum should appear at $\theta = 0^\circ$. This local extremum cannot be utilized to deduce emission zone properties as it is always present due to the symmetrical nature of the emission pattern (Eq. (1)); considering nearby identified local extrema increases the risk that experimental errors which deteriorate this symmetry will become pronounced. At large observation angles $|\theta| > 80^\circ$, the measured data are usually less reliable due to low intensity and possible contributions of edge emission, thus we disregard this angular region as well.
2. Only one local extremum of each class (local maximum or local minimum) is allowed in the range $[10^\circ, 80^\circ]$. As it is not probable to discover more than one local extremum of each class in IS interference patterns produced by OLEDs with typical emitter-cathode separation distances, if such a case is encountered, the emission pattern at the wavelength under consideration will not be processed as we assume the cause for this discrepancy is a high noise level.
3. Due to the symmetry requirement of the emission pattern noted in item 1 above, we only consider an identified local extremum $\theta_{\text{ex}} \in [10^\circ, 80^\circ]$ to be proper if a corresponding local extremum $-\theta_{\text{ex}} + \Delta\theta$ is identified in the interval $[-80^\circ, -10^\circ]$ within an allowed tolerance of $|\Delta\theta| < 5^\circ$. As in item 2, deviation from this symmetry condition is an indication for a noisy measurement at this wavelength, and this local extremum will not be processed for EZ estimation.

¹M. A. Baldo, M. E. Thompson, and S. R. Forrest, *Nature* **403**, 750 (2000).

²D. Reineke, F. Lindner, G. Schwartz, N. Seidler, K. Walzer, B. Lüssem, and K. Leo, *Nature* **459**, 234 (2009).

³M. Thomschke, S. Hofmann, S. Olthof, M. Anderson, H. Kleemann, M. Schober, B. Lüssem, and K. Leo, *Appl. Phys. Lett.* **98**, 083304 (2011).

⁴R. Meerheim, M. Furno, S. Hofmann, B. Lüssem, and K. Leo, *Appl. Phys. Lett.* **97**, 253305 (2010).

⁵W. Brütting, J. Frischeisen, T. D. Schmidt, B. J. Scholz, and C. Mayr, *Phys. Status Solidi A* **210**, 44 (2013).

⁶K. A. Neyts, *J. Opt. Soc. Am. A* **15**, 962 (1998).

⁷N. Tessler, *Appl. Phys. Lett.* **77**, 1897 (2000).

⁸C.-L. Lin, T.-Y. Cho, C.-H. Chang, and C.-C. Wu, *Appl. Phys. Lett.* **88**, 081114 (2006).

⁹A. Epstein, N. Tessler, and P. D. Einziger, *IEEE J. Quantum Electron.* **46**, 1388 (2010).

¹⁰J. Frischeisen, D. Yokoyama, A. Endo, C. Adachi, and W. Brütting, *Org. Electron.* **12**, 809 (2011).

¹¹M. Furno, R. Meerheim, S. Hofmann, B. Lüssem, and K. Leo, *Phys. Rev. B* **85**, 115205 (2012).

¹²T. D. Schmidt, D. S. Setz, M. Flämmich, J. Frischeisen, D. Michaelis, C. Mayr, A. F. Rausch, T. Wehler, B. J. Scholz, T. C. G. Reusch, N. Danz, and W. Brütting, *Appl. Phys. Lett.* **103**, 093303 (2013).

¹³N. Tessler, X.-C. Li, R. Friend, S. Morra, and A. Holmes, *Synth. Met.* **102**, 1124 (1999).

¹⁴M. Mesta, M. Carvelli, R. J. de Vries, H. van Eersel, J. J. M. van der Holst, M. Schober, M. Furno, B. Lüssem, K. Leo, P. Loebl, R. Coehoorn, and P. A. Bobbert, *Nature Mater.* **12**, 652 (2013).

¹⁵T. Granlund, L. Pettersson, and O. Inganäs, *J. Appl. Phys.* **89**, 5897 (2001).

¹⁶M. C. Gather, M. Flämmich, N. Danz, D. Michaelis, and K. Meerholz, *Appl. Phys. Lett.* **94**, 263301 (2009).

¹⁷B. Perucco, N. A. Reinke, D. Rezzonico, M. Moos, and B. Ruhstaller, *Opt. Express* **18**, A246 (2010).

¹⁸M. Flämmich, M. C. Gather, N. Danz, D. Michaelis, A. H. Bräuer, K. Meerholz, and A. Tünnermann, *Org. Electron.* **11**, 1039 (2010).

¹⁹S. L. M. van Mensfoort, M. Carvelli, M. Megens, D. Wehenkel, M. Bartzel, H. Greiner, R. A. J. Janssen, and R. Coehoorn, *Nat. Photonics* **4**, 329 (2010).

²⁰M. Flämmich, D. Michaelis, and N. Danz, *Org. Electron.* **12**, 83 (2011).

²¹L. Penninck, F. Steinbacher, R. Krause, and K. Neyts, *Org. Electron.* **13**, 3079 (2012).

²²N. Danz, M. Flämmich, D. S. Setz, B. C. Krummacher, D. Michaelis, and T. Dobbertin, *Opt. Lett.* **37**, 4134 (2012).

²³M. Carvelli, R. A. J. Janssen, and R. Coehoorn, *J. Appl. Phys.* **110**, 084512 (2011).

²⁴A. Epstein, N. Tessler, and P. D. Einziger, *Opt. Lett.* **35**, 3366 (2010).

²⁵See <http://webee.technion.ac.il/labs/orgelect/WhereIsMyEmissionZone.html> for a simple applet based on our method based on raw measured emission patterns.

²⁶We have recently proven that the transverse electric (TE) polarized emission patterns predicted by the simplified formulation match *exactly* those of the realistic devices, thus ensuring the validity of our previous results.^{30,31} Nonetheless, the transverse magnetic (TM) polarized emission contains further information regarding the orientation distribution of the emitting dipoles; in order to utilize it, the 3D model should be used.

²⁷TE-polarized emission is defined as the contribution to the total emission arising from electromagnetic fields in which the electric field is parallel to the OLED layer interfaces. Similarly, TM-polarized emission is produced by electromagnetic fields in which the magnetic field is parallel to the OLED layer interfaces. The two contributions are orthogonal.

²⁸P. Liehm, C. Murawski, M. Furno, B. Lüssem, K. Leo, and M. C. Gather, *Appl. Phys. Lett.* **101**, 253304 (2012).

²⁹A. Epstein, N. Tessler, and P. D. Einziger, *Opt. Express* **20**, 7929 (2012).

³⁰A. Epstein and P. D. Einziger, in *Proceedings of the 7th European Conference on Antennas and Propagation (EuCAP2013)* (IEEE, 2013), pp. 1026–1030.

³¹A. Epstein, N. Tessler, and P. D. Einziger, in *Proceedings of the URSI Commission B 2013 International Symposium on Electromagnetic Theory (EMTS2013)* (2013), pp. 1031–1034.

³²L. B. Felsen and N. Marcuvitz, *Radiation and Scattering of Waves*, 1st ed. (Prentice-Hall, Englewood Cliffs, NJ, 1973).

³³W. Lukosz, *J. Opt. Soc. Am.* **69**, 1495 (1979).

³⁴H. Benisty, R. Stanley, and M. Mayer, *J. Opt. Soc. Am. A* **15**, 1192 (1998).

³⁵D. Sokolik, “Power absorption in highly lossy biological tissues: electric dipole excitation,” Master’s thesis (Technion-Israel Institute of Technology, 2003).

³⁶The difference in definitions is due to the fact that for $n > 0$, the n th interface d_n separates the n th and $(n + 1)$ th layers, while for $n < 0$ the n th interface separates the n th and $(n - 1)$ th layers (Fig. 1).

³⁷A. Epstein, N. Tessler, and P. D. Einziger, *Phys. Rev. A* **87**, 043844 (2013).

³⁸K. Saxena, D. S. Mehta, R. Srivastava, and M. N. Kamalasanan, *Appl. Phys. Lett.* **89**, 061124 (2006).

³⁹D. Razansky, D. F. Soldea, and P. D. Einziger, *J. Appl. Phys.* **95**, 8298 (2004).

- ⁴⁰H. Kim, C. M. Gilmore, A. Pique, J. S. Horwitz, H. Mattoussi, H. Murata, Z. H. Kafafi, and D. B. Chrisey, *J. Appl. Phys.* **86**, 6451 (1999).
- ⁴¹P. A. Hobson, J. A. E. Wasey, I. Sage, and W. L. Barnes, *IEEE J. Sel. Top. Quantum Electron.* **8**, 378 (2002).
- ⁴²M. Flämmich, M. C. Gather, N. Danz, D. Michaelis, and K. Meerholz, *Appl. Phys. Lett.* **95**, 263306 (2009).
- ⁴³M. Weber, *Handbook of Optical Materials* (CRC Press, Boca Raton, 2003).
- ⁴⁴M. Roberts, K. Asada, M. Cass, C. Coward, S. King, A. Lee, M. Pintani, M. Ramon, and C. Foden, *Proc. SPIE* **7722**, 77220C (2010).
- ⁴⁵See <http://webee.technion.ac.il/orgelect/whereIsMyEmissionZonePP.html> for a bundle of MATLAB scripts implementing the evaluation procedure presented herein including preprocessing of the emission patterns to isolate the image-source interference pattern.
- ⁴⁶A. A. Shcherbakov, A. V. Tishchenko, D. S. Setz, and B. C. Krummacher, *Org. Electron.* **12**, 654 (2011).
- ⁴⁷A. Epstein, N. Tessler, and P. Einziger, in *Proceedings of the 2012 IEEE International Symposium on Antennas and Propagation (APS/URSI)* (2012), pp. 1–2.
- ⁴⁸C.-H. Tsai, K.-C. Tien, M.-C. Chen, K.-M. Chang, M.-S. Lin, H.-C. Cheng, Y.-H. Lin, H.-W. Chang, H.-W. Lin, C.-L. Lin, and C.-C. Wu, *Org. Electron.* **11**, 439 (2010).
- ⁴⁹S. Mladenovski, K. Neyts, D. Pavicic, A. Werner, and C. Rothe, *Opt. Express* **17**, 7562 (2009).
- ⁵⁰Z. B. Wang, M. G. Helander, J. Qiu, D. P. Puzzo, M. T. Greiner, Z. M. Hudson, S. Wang, Z. W. Liu, and Z. H. Lu, *Nat. Photonics* **5**, 753 (2011).
- ⁵¹The difference between the procedures is that now the orientation factor of the VEDs $M_{\zeta^{\perp}}^M$ (Eq. (8)) should be considered in the evaluation of IS contribution to the emission pattern (Eq. (12)), and the phase induced by the reflection from the cathode ($\alpha_{\text{img}} - \alpha_0$), which appears in Eq. (23) should be suitable for a TM reflection coefficient.²⁴ Moreover, in Eqs. (24)–(27), the side-lobe emission should be compared to the emission to an angle $\theta \neq 0$, as VEDs do not emit in the forward direction.